Coordination of Pickpocket ion channel delivery and dendrite growth in Drosophila sensory neurons

Josephine W. Mitchell[1,2], Ipek Midillioglu[3,*], Ethan Schauer[3,*], Bei Wang[4,5], Chun Han[4,5], and Jill Wildonger[2,3,6,^]

[1]Integrated Program in Biochemistry, University of Wisconsin-Madison, Madison, WI, USA

[2]Biochemistry Department, University of Wisconsin-Madison, Madison, WI, USA

[3]Pediatrics Department, University of California, San Diego, La Jolla, CA, USA

[4]Weill Institute for Cell and Molecular Biology, Cornell University, Ithaca, NY, USA

[5]Department of Molecular Biology and Genetics, Cornell University, Ithaca, NY, USA

[6]Cell & Developmental Biology, School of Biological Sciences, University of California, San Diego, La Jolla, CA, USA

*Equal contribution

^Corresponding author

Email: jwildonger@ucsd.edu (JW)

Abbreviations: Degenerin/Epithelial Na^+ Channel/Acid Sensing Ion Channels (DEG/ENaC/ASICs), dendritic arborization (da), dominant-negative (DN), dynamitin (dmn), Dynein light intermediate chain (Dlic), Ecdysone receptor (EcR), endoplasmic reticulum (ER), extracellular (EC), fluorescence recovery after photobleaching (FRAP), guide RNA (gRNA), phosphoinositide 3-kinase (PI3K), lava lamp (lva), over-expressing (O/E), Pickpocket (Ppk), superfolder GFP (sfGFP), secreted GFP (secGFP), Transient Receptor Potential (TRP)

Abstract

Sensory neurons enable an organism to perceive external stimuli, which is essential for survival. The sensory capacity of a neuron depends on the elaboration of its dendritic arbor and the delivery of sensory ion channels to the dendritic membrane. However, it is not well understood how ion channels are trafficked to sensory dendrites and whether their delivery is coordinated with dendrite growth. We investigated the trafficking of the DEG/ENaC/ASIC ion channel Pickpocket (Ppk) in peripheral sensory neurons in fruit fly larvae. We used CRISPR-Cas9 genome engineering to tag endogenous Ppk1 and visualize it live, including monitoring Ppk1 membrane localization via a novel secreted split-GFP approach. Strikingly, Ppk1 is present throughout the membrane of actively growing dendrites, and Ppk1 density scales in proportion to the dendritic membrane, even when dynein-mediated transport to dendrites is disrupted. Our data suggest that Ppk1 is integral to the membrane of growing dendrites and implicate the recycling endosome GTPase Rab11 in the forward trafficking of Ppk1 to dendrites. Together, our results suggest that Ppk channel transport is coordinated with dendrite morphogenesis, thus ensuring proper ion channel levels and distribution in sensory dendrites.

Author Summary

Peripheral sensory neurons are essential for an organism to interact with its environment. Neurons are composed of signal-receiving dendrites and a signal-sending axon. Ion channels distributed throughout sensory dendrites transduce external stimuli into chemical signals, however the mechanisms that localize ion channels to sensory dendrites are not well understood. Both the composition of ion channels in the dendrites and the structure of a sensory neuron's dendritic arbor are important for how it functions to sense external stimuli. Using live imaging and genomic engineering, we have discovered that the localization of a sensory ion channel, Pickpocket, in fruit fly sensory neurons is coordinated with growth of the dendritic arbor and that Pickpocket levels scale in proportion to dendrite length, even when transport to dendrites is disrupted. We also developed a novel genetically encoded approach to visualize the membrane expression of proteins in a living organism utilizing the split-GFP system. We found that both the secretory and endosomal networks mediate the forward trafficking of Pickpocket during neuronal morphogenesis, thus coordinating membrane growth with ion channel delivery. Our findings reveal that actively growing sensory dendrites are equipped with the ion channels needed for sensing external stimuli.

Introduction

An organism's interactions with its environment rely on its ability to sense external stimuli through sensory neurons. Ion channels distributed throughout the dendritic arbor of a sensory neuron rapidly transduce external stimuli into cellular signals. Both the morphology of a sensory neuron's dendritic arbor and the localization of ion channels in the arbor are essential to the establishment of a neuron's receptive field and sensory capacity. While the localization of ion channels to synapses in the central nervous system has been well studied [1], little is known regarding mechanisms that regulate the delivery of ion channels to the dendritic membrane of sensory neurons in the peripheral nervous system. It is also not known whether and how this trafficking may be coordinated with dendrite morphogenesis to establish the proper distribution of ion channels needed for sensing environmental stimuli.

To investigate the relationship between ion channel trafficking and dendrite growth, we used the *Drosophila melanogaster* class IV dendritic arborization (da) neurons as a model. The class IV da neurons function as polymodal nociceptors that detect multiple stimuli (thermal, mechanical, and light) and extend elaborately branched dendritic arbors that cover the larval body wall [2–5]. These neurons are an ideal model to study ion channel delivery in growing sensory dendrites for several reasons. First, during larval development, the class IV da neuron dendrites undergo expansive growth that can be easily visualized live in intact animals due to their superficial location just beneath the transparent larval cuticle and their relatively flat, two-dimensional morphology [6,7]. Second, the class IV da neurons have been a powerful *in vivo* model to identify mechanisms of dendrite morphogenesis, including players involved in membrane production and trafficking, the secretory and endosomal networks, molecular motor-based transport, and the cytoskeleton [8,9]. By manipulating known mechanisms of dendrite arbor growth, we can investigate how ion channel trafficking is coordinated with dendrite morphogenesis. Third, the general morphology and function of the class IV neurons is similar to

83 peripheral sensory neurons and nociceptors in other organisms, including the mammalian C-
84 and Aδ-fibers and the worm PVD and FLP neurons [10–12]. Thus, studying ion channel
85 trafficking in the class IV da neurons may shed light on conserved mechanisms of ion channel
86 localization in sensory dendrites.
87
88 During neuronal morphogenesis, the class IV da neurons express several dendritic ion channels
89 that have been structurally and functionally characterized, including Pickpocket (Ppk); Transient
90 Receptor Potential (TRP) channels, such as painless; and Piezo [3,13–16]. Whereas TRP and
91 Piezo channels are comprised of large multi-pass membrane protein subunits, the Ppk ion
92 channel subunits are relatively small, two-pass membrane proteins. Their modest size makes
93 endogenous Ppk channels amenable to manipulation via CRISPR-Cas9 genome engineering.
94 Moreover, the crystal structure of a conserved Ppk ortholog in chickens, ASIC1, has been
95 solved, and this information is advantageous for the structure-guided manipulation of Ppk [17].
96 For these reasons we decided to focus on investigating the trafficking of Ppk in the class IV da
97 neurons.
98
99 Ppk proteins belong to the large, structurally conserved family of Degenerin/Epithelial Na^+
100 Channel/Acid Sensing Ion Channels (DEG/ENaC/ASICs) whose members in worms, flies, fish,
101 and mammals carry out a variety of functions ranging from mechanosensation and learning and
102 memory in the nervous system to salt homeostasis in epithelial cells in the kidney [18–20]. In
103 the fly class IV da neurons, the Ppk channel is composed of two subunits, Pickpocket 1 (Ppk1)
104 and Pickpocket 26 (Ppk26), which are mutually dependent on each other for membrane
105 expression [16,21–23]. The localization of Ppk1 and Ppk26 has been characterized using
106 antibodies and fluorescently tagged transgenes, and both subunits are broadly distributed
107 throughout the developing dendrites of class IV da neurons. Interestingly, Ppk1 and Ppk26 are
108 expressed from late-embryo to mid-larval stages, which coincides with a period of rapid dendrite

growth [6,16,21,24–26]. The timing of Ppk1 and Ppk26 expression suggests that Ppk channel production and localization may be coordinated with dendrite growth.

To investigate the potential coordination of Ppk1 trafficking and dendrite growth, we used CRISPR-Cas9 genome engineering to tag endogenous Ppk1 and follow its localization in growing dendrites. We found that in developing neurons, Ppk1 is enriched throughout dendrites and is also present in axon terminals and at low levels in axons. Using a new split-GFP strategy to monitor the insertion of proteins into the cell membrane, we visualized Ppk1 membrane expression live in developing neurons, which revealed the robust, uniform membrane localization of Ppk1 in the somatodendritic compartment. We found that Ppk1 was present throughout growing dendrite branches and in actively growing dendrite tips, suggesting that Ppk1 is part of the nascent membrane that is adding to growing dendrites. In support of this model, we found that Ppk1 dendritic levels scale in proportion to the amount of dendritic membrane, even when transport to dendrites is disrupted by perturbing dynein. We also discovered that the recycling endosome GTPase Rab11 is involved in forward trafficking of Ppk1 to dendrites, which indicates a role for endosome-mediated trafficking in both dendrite growth and the delivery of a sensory ion channel. Together, our results suggest that Ppk channel delivery is coordinated with sensory dendrite morphogenesis, thus revealing a mechanism to establish proper ion channel levels and distribution throughout sensory dendrites.

Results

Ppk1 is enriched in dendrites and the dendritic membrane in developing sensory neurons

To visualize the localization of the Ppk ion channel in sensory neurons, we tagged endogenous Ppk1 with fluorescent proteins. To facilitate the manipulation of *ppk1*, we first replaced the ppk1 gene with an attP "docking site," which enables the reliable and rapid knock-in of new *ppk1* alleles (Fig 1A). We then used this strain to knock-in *ppk1* tagged with one copy of superfolder GFP (sfGFP) at either the N- or C-terminus (Fig 1B and S1 Fig; since Ppk1 tagged with GFP at either terminus displayed similar localization, we used C-terminally tagged Ppk1 for most of our experiments). Excitingly, we observed fluorescent signal in neurons in live animals with just one copy of GFP attached to Ppk1 (Fig 1B). Consistent with previous reports, Ppk1::sfGFP was expressed in the class IV da neurons in the peripheral nervous system [2,16,25]. In the dorsal class IV da neuron called ddaC, Ppk1::sfGFP localized to both dendrites and axons, but its distribution to and within these compartments differed. Ppk1::sfGFP was enriched in dendrites, where it appeared to localize predominantly to the dendritic membrane and was present throughout the dendritic arbor (Fig 1B). This distribution matches the previously reported distribution of Ppk1 based on antibody staining and fluorescently tagged Ppk1 transgenes [21,23,27]. In contrast to dendrites, the Ppk1::sfGFP signal was dimmer in axons and did not align with the axonal membrane (Fig 1B). In the ventral nerve cord, where the ddaC axons terminate, Ppk1::sfGFP was present in axon terminals (Fig 1C). Altogether, our data indicate that Ppk1::sfGFP localizes predominantly to dendrites, but that it is also present at low levels in axons and in axon terminals.

In addition to tagging Ppk1 with sfGFP, we also tagged Ppk1 with mCherry at the C-terminus. The distribution of Ppk1::mCherry was similar to Ppk1::sfGFP in dendrites and axons (Fig 1D).

154 There was, however, a striking difference: unlike Ppk1::sfGFP, Ppk1::mCherry clustered in
155 bright puncta that concentrated in the cell body, proximal dendrites, and axon (Fig 1D and 1G).
156 These Ppk1::mCherry puncta were motile and moved at speeds consistent with microtubule-
157 based transport (Fig 1E). This is in contrast with Ppk1::sfGFP, which was rarely visible in puncta
158 (Fig 1B). Interestingly, the Ppk1 partner subunit Ppk26 tagged with the fluorescent protein
159 Dendra2 also displays a punctate distribution pattern similar to mCherry-tagged Ppk1, whereas
160 Ppk26 tagged with GFP resembles the more uniform distribution of GFP-tagged Ppk1 [23,28].
161 Unsure of whether the mCherry tag might direct Ppk1 to a different compartment than sfGFP,
162 we next generated Ppk1 tagged with both sfGFP and mCherry (sfGFP::Ppk1::mCherry). The
163 sfGFP and mCherry fluorescent signals of the dual-tagged sfGFP::Ppk1::mCherry resembled
164 those of the singly tagged Ppk1 proteins (Fig 1F and 1G). This suggests that the punctate
165 mCherry signal does not reflect a difference in the localization of mCherry-tagged Ppk1. Rather,
166 the mCherry tag may reveal the localization of Ppk1 to a compartment(s) where sfGFP does not
167 fluoresce. For example, among other differences, sfGFP and mCherry have different maturation
168 kinetics and are differentially sensitive to pH (e.g., GFP fluorescence is quenched by low pH
169 whereas mCherry is not) [29]. Indeed, these differences in fluorescent protein properties have
170 been leveraged to monitor the subcellular distribution of the transmembrane protein Notch [30].
171 Our comparison of the fluorescent sfGFP and mCherry signals of the dual-tagged Ppk1
172 indicates that the identity of the fluorescent protein tag can influence protein visualization and
173 that using different fluorescent tags may be necessary to visualize the full potential range of a
174 protein's localization in cells.
175
176 The localization of fluorescently tagged Ppk1 to both axons and dendrites raises the question of
177 where Ppk1 is inserted into the membrane. To monitor the membrane localization of Ppk1, we
178 initially tagged Ppk1 with superecliptic pHluorin. Superecliptic pHluorin (referred to simply as
179 pHluorin hereafter) is a pH-sensitive GFP variant that is often used to monitor the insertion of

180 transmembrane proteins because it fluoresces in neutral pH environments, such as extracellular
181 space, but has minimal fluorescence in low pH environments, such as the lumen of a transport
182 vesicle [31]. To determine an optimal extracellular position at which to add a fluorescent tag
183 such as pHluorin, we first tagged an extracellular loop of endogenous Ppk1 with sfGFP and
184 compared its fluorescence to Ppk1 tagged with sfGFP at the N- or C-terminus. We tested two
185 positions in an extracellular (EC) loop: Site 1 was selected based on the structure of chicken
186 ASIC1, and Site 2 is a position that was previously used to monitor rat ASIC1a membrane
187 insertion via a haemagglutinin epitope tag [32] (S2 Fig). We found that insertion of sfGFP at Site
188 1 resulted in fluorescence similar to Ppk1::sfGFP, whereas the insertion of sfGFP at Site 2 led
189 to relatively weak fluorescence (S2 Fig). We then tagged Ppk1 with pHluorin at Site 1 and found
190 that Ppk1::pHluorin^{EC} produced relatively weak fluorescence (S2 Fig). We next tested the
191 effects of eliminating Ppk26 on Ppk1::pHluorin^{EC} fluorescence and distribution, as the loss of
192 Ppk26 should interfere with the membrane localization of Ppk1. In *ppk26* mutant neurons,
193 Ppk1::pHluorin^{EC} fluorescence noticeably increased in the cell body and decreased in dendrites,
194 but fluorescence was still clearly visible in patches in dendrites, particularly at dendrite branch
195 points (S2 Fig). Given that the membrane localization of Ppk1 depends on Ppk26, the
196 fluorescence pattern of Ppk1::pHluorin^{EC} in the *Ppk26* mutant neurons suggested that
197 Ppk1::pHluorin^{EC} might fluoresce in the neutral environment of the endoplasmic reticulum (ER)
198 as well as in the cell membrane. The potential for Ppk1::pHluorin^{EC} to fluoresce in both the ER
199 and cell membrane limits its use as a tool to monitor the insertion of Ppk1 into the neuronal
200 membrane.
201
202 The weak fluorescent signal of Ppk1::pHluorin^{EC}, and its ability to fluoresce in the ER, led us to
203 develop a new split-GFP approach to monitor the membrane insertion of endogenous Ppk1 (Fig
204 2A). This approach is analogous to other recently reported split-GFP techniques to monitor the
205 localization of transmembrane proteins [33,34]. We tagged endogenous Ppk1 at Site 1 in the

206 extracellular loop with three copies of the split-GFP peptide GFP(11). In addition to the
207 extracellular GFP(11) tag, we also tagged the Ppk1 C-terminus with mCherry, which enabled us
208 to follow Ppk1 localization throughout the neuron (Ppk1::GFP(11x3)^{EC}::mCherry$^{C\text{-}term}$). We then
209 expressed a secreted version of GFP(1-10) (secGFP(1-10)) in fat cells, which released
210 secGFP(1-10) into the hemolymph of the larval open circulatory system. Thus, Ppk1 tagged with
211 GFP(11) in an extracellular loop will only fluoresce when Ppk1 is inserted into the cell
212 membrane and encounters secGFP(1-10) (S3 Fig). As a control, we used a construct in which
213 the extracellular N-terminus of the single-pass transmembrane protein CD4 is tagged with
214 GFP(11) and the C-terminus is tagged with tdTomato (GFP(11)^{EC}::CD4::tdTomato) (S4 Fig)
215 [35].
216
217 Using this split-GFP approach, we monitored GFP fluorescence from Ppk1 and CD4 tagged
218 with GFP(11). Both Ppk1::GFP(11x3)^{EC}::mCherry$^{C\text{-}term}$ and GFP(11)^{EC}::CD4::tdTomato exhibited
219 GFP fluorescence in dendrites and cell bodies (Fig 2B, 2C and 2D, and S4 Fig). As described
220 above, the membrane localization of Ppk1 depends on Ppk26 [21–23]. In neurons lacking
221 Ppk26, there was no GFP fluorescent signal from Ppk1::GFP(11x3)^{EC}::mCherry$^{C\text{-}term}$, albeit the
222 mCherry signal was still visible, indicating that Ppk1 was still produced in the absence of Ppk26
223 (Fig 2B). These results support the idea that GFP fluorescence results from Ppk1 insertion into
224 the dendritic membrane.
225
226 Next, we examined axons and axon terminals. Strikingly, in neurons expressing Ppk1 tagged
227 with GFP(11), we observed a distinct boundary of GFP fluorescence between the cell body and
228 proximal axon, the latter of which was devoid of fluorescent signal (Fig 2D). While the proximal
229 axon and axon shaft lacked GFP fluorescence, we observed GFP fluorescence in the axon
230 terminals of neurons expressing Ppk1::GFP(11x3)^{EC}::mCherry$^{C\text{-}term}$ (Fig 2E). The peripheral
231 axons and ventral nerve cord are wrapped by glia, which form a barrier that is unlikely to be

232 penetrated by secGFP(1-10) [36–38]. Thus, the GFP fluorescence from Ppk1 tagged with
233 GFP(11) potentially reflects the trans-endocytosis of Ppk1 from the somatodendritic
234 compartment to the axon terminals.
235
236 In contrast to Ppk1 tagged with GFP(11), CD4 tagged with GFP(11) displayed GFP
237 fluorescence throughout the proximal axon and axon shaft (Fig 2D). This indicates a difference
238 in the membrane localization of endogenous Ppk1 and CD4. In summary, we have developed a
239 new assay to monitor the neuronal membrane localization of Ppk1, which we have used to
240 reveal that Ppk1 is inserted into the somatodendritic membrane and the axon terminal
241 membrane but not the membrane in the proximal axon or axon shaft.
242
243 **Ppk1 is present in dendritic branches as they form and extend**
244 The localization of Ppk1 and Ppk channels throughout the dendritic arbor raises the question of
245 how Ppk1 becomes so broadly localized. One possibility is that Ppk1 is delivered to dendrites at
246 the same time that the arbor is established, and thus Ppk1 distribution may be coordinated with
247 dendrite growth. To determine the localization of Ppk1 relative to when they develop, we
248 examined the early expression of Ppk1. *ppk1* expression is reported to initiate during embryonic
249 stages, slightly before dendrites emerge (~embryonic stage 16) [16,21,24–26]. Indeed, we first
250 observed Ppk1::sfGFP in cell bodies and proximal axons just prior to dendrite extension, and we
251 even observe Ppk1::sfGFP in newly emerging dendrites (Fig 3A). These data indicate that Ppk1
252 is expressed from the very beginning of dendritogenesis.
253
254 Next, we asked whether Ppk1 is present in growing dendrites. Since imaging Ppk1::sfGFP
255 during embryonic stages was technically challenging, we followed the real-time localization of
256 Ppk1::sfGFP in both newly formed and extending dendrite branches in larvae. Strikingly,
257 Ppk1::sfGFP was present throughout growing dendrite branches, in both branches that formed

258 *de novo* and branches that extended (Fig 3B). We imaged Ppk1::sfGFP both continuously and
259 over a period of several minutes, and at both time scales we consistently observed Ppk1::sfGFP
260 throughout dendrite branches as they grew and, in some instances, retracted. We also imaged
261 Ppk1 tagged with GFP(11) and observed GFP fluorescence in growing dendrite branches, which
262 indicates that Ppk1 is integral to the membrane of growing dendrite tips (Fig 3C). Altogether,
263 these data indicate that Ppk1 is present in growing dendrites.
264
265 We next asked whether the broad distribution of Ppk1 throughout the dendritic arbor and in
266 growing dendrites might reflect its ability to readily diffuse in the dendritic membrane. To test
267 this we carried out fluorescence recovery after photobleaching (FRAP) with GFP(11)-tagged
268 Ppk1 and CD4 (Ppk1::GFP(11x3)^{EC}::mCherry$^{C\text{-term}}$ and GFP(11)^{EC}::CD4::tdTomato,
269 respectively). After photobleaching, GFP fluorescence from Ppk1::GFP(11x3)^{EC}::mCherry$^{C\text{-term}}$
270 recovered gradually over tens of minutes, significantly slower than GFP(11)^{EC}::CD4::tdTomato
271 (Fig 3D). These FRAP results indicate that rapid diffusion of Ppk1 is unlikely to explain its broad
272 distribution and presence in growing dendrites.
273
274 Our findings that Ppk1 is present in growing dendrites raises the question of whether Ppk1, and
275 its partner subunit Ppk26, are necessary for dendrite growth and whether any change in Ppk
276 channel activity might perturb dendrite morphogenesis. In neurons lacking both Ppk1 and
277 Ppk26, dendrite growth was normal (Fig 3E). Although the Ppk channel is not essential for
278 dendrite growth, we found, consistent with previous reports, that dendrite arborization is
279 reduced when Ppk channel activity is altered by a degenerin mutation in Ppk26, which keeps
280 the channel in an aberrant open state (S5 Fig) [18,21,39,40]. Surprisingly, the loss of Ppk1
281 enhanced, rather than suppressed, the reduction in dendrite arborization associated with the
282 mutant Ppk26 (S5 Fig). This suggests that the Ppk26 degenerin mutant does not depend on
283 Ppk1 to form a functional channel and that Ppk1 may restrain the activity of the mutant Ppk26.

284 Our data also suggest that either the mutant Ppk26 may be able to reach the dendritic
285 membrane independently of Ppk1 or that the dendrite growth defect caused by the Ppk26
286 degenerin mutant is due to the aberrant activity of Ppk26 in an internal organelle. Combined,
287 our results indicate that while Ppk1 and Ppk26 are dispensable for normal dendrite growth, Ppk
288 channel activity must be tightly regulated to achieve proper dendrite arborization.
289

290 **Ppk1 levels are not affected by decreasing dendrite arbor size but are reduced when**
291 **dendrite length significantly increases**

292 Our data reveal that Ppk1 is present in the membrane of extending dendrite branches. One
293 potential model based on these data is that Ppk1 is transported to dendrites via the membrane
294 that grows the dendritic arbor. Since we were not able to visualize the transport of fluorescently
295 tagged Ppk1 in growing dendrites, we instead considered the predictions of this model. One
296 prediction of the model that Ppk1 is transported to dendrites with the membrane that grows the
297 arbor is that the dendritic levels of Ppk1 should be proportional to the amount of dendritic
298 membrane or, in other words, dendrite size. We tested this by assessing Ppk1 levels when
299 dendrite arbor size was altered. We took advantage of different conditions that are known to
300 reduce or increase dendrite growth, acknowledging that these experiments could only serve as
301 a general test of whether Ppk1 levels are proportional to dendrite arbor size. First, we tested two
302 different conditions that reduce dendrite growth: knock-down of the ribosomal protein Rpl22 and
303 overexpression of the ecdysone receptor (EcR) [41,42]. Under both conditions, Ppk1::sfGFP
304 density in dendrites was similar to controls, supporting the idea that Ppk1 levels were
305 proportional to arbor size when dendrite growth was reduced by these two manipulations (Fig
306 4A and 4B). We then determined whether Ppk1 levels would change when dendrite growth
307 increased using the overexpression of the actin regulator Rac1 [43] and the overexpression of
308 phosphoinositide 3-kinase (PI3K), which regulates cell growth through the mTOR (mechanistic
309 target of rapamycin) pathway [6]. As previously reported, Rac1 overexpression increased

310 dendrite branch number without affecting dendrite length, and we found that Ppk1::sfGFP levels
311 were not affected (Fig 4C). Overexpression of PI3K increased both dendrite branch number and
312 dendrite length by approximately a third, and, in contrast to the other growth-perturbing
313 conditions, Ppk1::sfGFP levels were reduced by nearly a third (Fig 4D). In this overgrowth
314 condition it is possible that the production of Ppk1::sfGFP is outpaced by dendrite growth.
315 Although this is only a small sampling of the many conditions that affect dendrite growth, our
316 results suggest that the dendritic levels of Ppk1 are not generally altered by perturbing dendrite
317 growth.
318
319 **Ppk1 persists in dendrites when dynein-mediated transport is perturbed**
320 We further tested the model that Ppk1 is transported to dendrites via the membrane that grows
321 the dendritic arbor by disrupting transport to dendrites. We reasoned that if Ppk1 is trafficked via
322 the membrane that fuels dendrite growth, then perturbing transport to dendrites should
323 decrease growth and have a proportional effect on the dendritic levels of Ppk1 (e.g., the density
324 of Ppk1 should not be affected).
325
326 We took several complementary approaches to determine the effects of disrupting dendritic
327 transport on Ppk1. Most transport to and within dendrites occurs along microtubules. In da
328 neuron dendrites, nearly all microtubules are oriented with their minus-ends positioned away
329 from the cell body [44]. Thus, the microtubule minus-end-directed motor dynein is thought to
330 mediate the majority of transport to dendrites. We perturbed dynein function in several ways.
331 First, we reduced the levels of the essential dynein subunit dynein light intermediate chain (Dlic)
332 via RNAi. In *Dlic-RNAi*-expressing neurons, we observed a reduction in dendrite growth as
333 previously reported [45,46], but dendritic Ppk1::sfGFP levels were similar to controls (Fig 5A).
334 Consistent with these results, we found that loss of the dynein co-factor nudE, which also
335 disrupts dendrite morphogenesis [47], did not affect the dendritic levels of Ppk1::sfGFP (control:

336 112.77 ± 21.05 arbitrary units [AU]; *nudE*^{39A}/*Df(3L)BSC673*: 110.52 ± 42.55 AU, mean ±
337 standard deviation; Student's unpaired t-test: p=0.8382; not significant). Thus, decreasing
338 dynein activity reduced dendrite growth, likely reflecting its role in dendritic transport, but Ppk1
339 levels in dendrites were unchanged. These results indicate that Ppk1 levels remain proportional
340 to dendrite arbor size in dynein loss-of-function neurons.
341
342 We also disrupted dynein activity by overexpressing dynamitin (dmn), a dynein co-factor and
343 dynactin complex member. Elevating dmn levels disrupts dynein activity, likely by perturbing
344 dynein-dynactin interactions [48,49]. Unlike *Dlic-RNAi* and *nudE* loss-of-function, the
345 overexpression of *dmn* reduced dendritic levels of Ppk1::sfGFP by approximately a quarter (Fig
346 5B). Since overexpressed dmn acts as a dominant-negative, it may exert a stronger, cumulative
347 effect on dynein-mediated transport than *Dlic-RNAi* and the *nudE* loss-of-function mutant.
348 Indeed, when we examined younger larvae, neurons overexpressing *dmn* had normal levels of
349 Ppk1::sfGFP (Fig 5B). Such a dose-dependent effect may also explain why we previously
350 observed reduced dendritic Ppk1 levels in clones of *dlic* mutant neurons, which completely lack
351 *dlic* [45]. Our results indicate that the overexpression of *dmn* initially had no effect on
352 Ppk1::sfGFP levels in dendrites but that the persistent overexpression of *dmn* resulted in the
353 decrease of Ppk1::sfGFP dendritic levels over time.
354
355 Our findings that the dendritic levels of Ppk1 are not affected by either *Dlic-RNAi* or *nudE* loss-
356 of-function could be interpreted to suggest that Ppk1 is not transported by dynein. To determine
357 whether dynein plays a role in transporting Ppk1 to dendrites, we took a closer look at neurons
358 expressing *Dlic-RNAi*. Most ion channels traffic through the Golgi apparatus, which, in the da
359 neurons, includes both the somatic Golgi and dendritic Golgi "outposts," which are Golgi mini-
360 stacks found predominantly in the proximal dendritic arbor [50–54]. In control neurons, we found
361 that Ppk1::sfGFP co-localized with somatic Golgi, although we did not detect any Ppk1::sfGFP

362 at dendritic Golgi outposts (Fig 5C). In neurons expressing *Dlic-RNAi*, Ppk1::sfGFP
363 accumulated at somatic Golgi and could also be observed at dendritic Golgi outposts. These
364 results suggest that Ppk1 traffics through both somatic Golgi and Golgi outposts and that Ppk1
365 is transported away from Golgi by dynein.
366
367 In addition to dendritic defects, neurons with altered dynein activity had increased levels of
368 Ppk1::sfGFP in axons (Fig 5A and 5B). Previous work by our group and others has shown that
369 Golgi and Golgi outposts mis-localize to axons when dynein activity is altered [45,47]. Given our
370 findings that Ppk1::sfGFP accumulates at Golgi in dynein loss-of-function neurons, one
371 possibility is that Ppk1::sfGFP "hitchhikes" on Golgi that are ectopically localized to axons.
372 However, in the axons of *Dlic-RNAi*-expressing neurons, Ppk1::sfGFP was often adjacent to,
373 but did not overlap with, the trans-Golgi marker GALNT2::TagRFP (Fig 5D). Although Ppk1 was
374 not hitchhiking on Golgi, it was still possible that the mis-localization of Golgi was responsible for
375 the increase in axonal Ppk1 levels. To test this, we perturbed the localization of Golgi by
376 disrupting the golgin lava lamp (lva), which links Golgi to dynein but otherwise does not
377 contribute to dynein activity [55,56]. Consistent with previous reports, we found that the
378 overexpression of dominant-negative lva resulted in the ectopic axonal localization of Golgi [52].
379 Lva dominant-negative also resulted in an increase in Ppk1::sfGFP levels in axons and the cell
380 body (Fig 5E). Combined, our results suggest that the mis-localization of Golgi in dynein loss-of-
381 function neurons is sufficient to result in the accumulation of Ppk1 in axons.
382
383 **Disrupting secretory pathway function impedes the delivery of Ppk1 to the dendritic**
384 **membrane**
385 Our finding that Ppk1 accumulates at Golgi when dynein function is perturbed indicates that
386 Ppk1 traffics through the Golgi, likely through both the somatic Golgi and Golgi outposts, before
387 being added to the growing dendritic membrane. Based on these data, we hypothesized that

interfering with the function of the secretory pathway, which is the predominant source of membrane for dendrite arbor growth and through which membrane proteins traffic, might reduce the dendritic levels of Ppk1. We disrupted secretory pathway function by impeding the budding of cargo-containing vesicles from the ER. We used a transgenic guide RNA (gRNA) that targets *Sec23*, which encodes an essential component of the COPII vesicular coat, in combination with a transgene that expresses Cas9 specifically in the class IV da neurons [57]. The *Sec23* gRNA targets the first coding exon of *Sec23* and, in combination with Cas9, is predicted to generate a loss-of-function allele by introducing a premature stop in Sec23. Indeed, neurons expressing *Sec23* gRNA and Cas9 had shorter dendrites and fewer branches, consistent with previously published work that *Sec23* loss-of-function reduces dendrite morphogenesis (Fig 6A) [52].

Next, we examined the effects of *Sec23* loss-of-function on Ppk1. *Sec23* loss-of-function neurons had significantly less membrane-associated Ppk1 as revealed by a reduction in GFP fluorescence from the dual-tagged Ppk1::GFP(11x3)^{EC}::mCherry$^{C\text{-term}}$ (Fig 6B). The mCherry fluorescence of Ppk1::GFP(11x3)^{EC}::mCherry$^{C\text{-term}}$ was also reduced, but to a lesser extent than the GFP fluorescence. This suggests that disrupting *Sec23* has only a modest effect on Ppk1 levels but has a severe effect on the trafficking of Ppk1 to the neuronal membrane. Consistent with this idea, the dendritic levels of Ppk1::sfGFP were not affected in *Sec23* loss-of-function neurons, although the pattern of Ppk1::sfGFP appeared patchy compared to its typical uniform distribution in control neurons (Fig 6C). Notably, both the mCherry fluorescence of Ppk1::GFP(11x3)^{EC}::mCherry$^{C\text{-term}}$ and the Ppk1::sfGFP fluorescence appeared greatly increased in the cell bodies (Fig 6B and 6C). Combined, these results suggest that perturbing *Sec23* results in dramatically less membrane-associated Ppk1 and likely causes an accumulation of Ppk1 at an early point during the secretory pathway, likely the ER.

Dendritic levels of Ppk1 are reduced by disrupting Rab11

414 We next asked what transport carriers might take Ppk1 from Golgi to growing dendrites and play
415 a role in coordinating ion channel delivery with dendrite growth. We considered Rab11-positive
416 endosomes for several reasons. First, Rab11 has been implicated in the anterograde trafficking
417 of ion channels to the dendritic membrane in mammalian neurons [58], and recent work
418 suggests that Rab11 may affect the trafficking of the Ppk1 partner subunit Ppk26 in fly da
419 neurons [28]. Additionally, Rab11 plays a role in the membrane localization of ENaC family
420 members in the epithelial cells of mammalian kidneys [59–61]. Rab11 mutants also reduce
421 dendrite arborization, indicating that it has a role in dendrite growth (S6 Fig) [28,62]. These data
422 suggest that Rab11 may play a role in both the dendritic localization of Ppk1 and dendrite arbor
423 development.
424
425 To test whether Rab11 indeed participates in trafficking Ppk1 to dendrites, we perturbed Rab11
426 function using both *Rab11-RNAi* and a dominant-negative Rab11 construct, Rab11-DN (Rab11-
427 DN carries an S25N mutation that disrupts GTPase activity). Knocking-down Rab11 with RNAi
428 decreased dendritic Ppk1 as determined by measuring Ppk1 membrane levels via
429 immunohistochemistry, Ppk1::sfGFP, and Ppk1::mCherry (Ppk1 membrane expression was
430 assayed with antibodies rather than GFP(11)-tagged Ppk1 for technical reasons; Fig 7A, 7B and
431 7C). In neurons expressing *Rab11-RNAi*, the decrease in Ppk1 in dendrites was accompanied
432 by an accumulation of Ppk1::sfGFP and Ppk1::mCherry in cell bodies (Fig 7B and 7C). Similar
433 to *Rab11-RNAi*, the overexpression of Rab11-DN also reduced Ppk1 levels in dendrites as
434 revealed by quantifying Ppk1 membrane expression via immunohistochemistry and
435 Ppk1::mCherry (Rab11-DN is tagged with GFP, and thus we were not able to quantify
436 Ppk1::GFP; Fig 7D and 7E). Like in neurons expressing *Rab11-RNAi*, Ppk1::mCherry
437 accumulated in the cell body in *Rab11-DN*-expressing neurons (Fig 7E). Together, these results
438 indicate that the disruption of Rab11 leads to a decrease in Ppk1 levels in dendrites and an
439 accumulation of Ppk1 in the cell body.

440

441 Our findings are consistent with the idea that Rab11 participates in transporting Ppk1 from Golgi
442 to dendrites, but Rab11 also plays a role in the local recycling of ion channels in dendrites [63].
443 We next asked whether dendritic Ppk1 levels might be regulated via local recycling. In addition
444 to Rab11, which functions in late recycling endosomes, local recycling of ion channels depends
445 on the early endosome GTPase Rab5 [63]. We found that dendritic Ppk1::mCherry puncta
446 colocalized with Rab5-positive early endosomes, as did some Ppk1::mCherry puncta in the cell
447 body, which suggests that Rab5 may play a role in trafficking Ppk1 (Fig 8A).
448

449 We next analyzed the effects of perturbing Rab5 function on dendritic levels of Ppk1 using a
450 dominant-negative Rab5 construct, Rab5-DN (Rab5-DN carries a S43N mutation that disrupts
451 GTPase activity). The overexpression of Rab5-DN did not disrupt dendritic levels of Ppk1 as
452 measured by quantifying Ppk1 dendritic membrane levels via immunohistochemistry and
453 Ppk1::mCherry (because Rab5-DN is tagged with YFP, we did not quantify GFP-tagged Ppk1)
454 (Fig 8B and 8C). Thus, although Rab5-DN reduces dendrite growth similar to Rab11-DN and
455 *Rab11-RNAi* (S6 Fig and S7 Fig), Rab5-DN has no effect on dendritic Ppk1 levels. Strikingly,
456 although the dendritic levels of Ppk1::mCherry were not affected by Rab5-DN, the number of
457 Ppk1::mCherry puncta in the proximal dendrites and cell body were significantly reduced, and,
458 in many neurons, virtually eliminated (Fig 8C). This suggests that Ppk1::mCherry puncta likely
459 represent Ppk1 in endosomes, specifically early endosomes whose formation depends on Rab5
460 function. Indeed, consistent with previous reports, we observed that fluorescently tagged Rab5-
461 DN appeared diffuse, which differed from the punctate distribution pattern of fluorescently
462 tagged wild-type Rab5 (S7 Fig) [64]. While this change in Rab5-DN distribution could reflect its
463 dissociation from early endosomes, it might also indicate that early endosome formation is
464 impaired in Rab5-DN-expressing neurons. Overall, our results suggest that Ppk1 traffics through
465 Rab5-positive endosomes but that this trafficking does not have a significant effect on dendritic

466 levels of Ppk1. Combined, our results suggest that Rab11 participates in the forward trafficking

467 of Ppk1 to dendrites at the same time that it promotes dendrite growth.

468 **Discussion**

469 The perception of stimuli by sensory neurons depends on the morphogenesis of a dendritic
470 arbor equipped with ion channels and receptors that will detect sensory inputs. Central
471 outstanding questions have been: How are ion channels and receptors localized to sensory
472 neuron dendrites during development, and how does a sensory neuron properly match ion
473 channel and receptor levels with dendrite arbor size? Sensory dendrites lack synaptic input,
474 which has made it unclear whether known mechanisms of ion channel and receptor trafficking to
475 dendrites with synapses would also regulate the delivery of ion channels and receptors to the
476 asynaptic dendrites of sensory neurons. Our studies of the localization of Ppk1 suggest a model
477 in which sensory neurons likely package ion channels into the membrane that grows the
478 dendritic arbor, thus coordinating the delivery of ion channels with arbor expansion.

479

480 Our data reveal that Ppk1 is present throughout the membrane of dendrites as they grow,
481 indicating that Ppk channels are an integral component of both newly formed and extending
482 dendrites. While the localization and function of ion channels in growing axons is well
483 established [65–71], little is still known about the localization and function of ion channels in
484 developing dendrites. The timing and breadth of Ppk1 distribution indicates that the class IV da
485 sensory dendrites are likely equipped with the capacity to detect stimuli as soon as dendrites
486 emerge. Indeed, recent work has implicated members of the *C. elegans* DEG/ENaC family in
487 sensing mechanical forces to promote terminal branch growth during arbor formation in PVD
488 neurons [72]. Although we found that dendrite development occurred normally without Ppk1 and
489 its partner subunit Ppk26, it is nonetheless possible that Ppk channels participate in dendrite
490 growth, possibly in collaboration with another (mechanosensory) ion channel. Class IV da
491 neurons express at least one additional mechanosensory channel, Piezo, whose worm ortholog
492 is only weakly expressed in PVD neurons. Knockdown of Piezo by RNAi reduces the growth of
493 class IV da neurons [73]. In vertebrate neurons, the distribution of ion channels in young

494 dendrites has been reported but is not well characterized, although a rich body of work supports
495 the role of activity in regulating dendrite growth [74–76]. Our visualization of fluorescently
496 tagged endogenous Ppk1 provides evidence that ion channels are indeed part of the growing
497 dendritic membrane, similar to the localization of ion channels in axons, and that sensory
498 dendrites thus have a "built in" capacity to detect stimuli.
499
500 The presence of Ppk1 in growing dendrites raises the possibility that Ppk channels are
501 transported to dendrites as part of the membrane that fuels arbor growth. In one test of this
502 model, we disrupted transport to dendrites by interfering with dynein. Dynein is the predominant
503 motor for dendritic transport in da neurons, and perturbing dynein function significantly reduces
504 arbor size [45,46]. We found that the dendritic levels of Ppk1::sfGFP remained normally
505 proportional to arbor size in neurons with reduced dynein activity. This suggests that in dynein
506 loss-of-function neurons, the membrane that does make it to dendrites has normal levels of
507 Ppk1. The finding that Ppk1::sfGFP accumulates at Golgi in dynein loss-of-function neurons
508 indicates that dynein normally transports Ppk1 (and Ppk channels) from Golgi to dendrites. Our
509 results, combined with previous studies [46], suggest that interfering with dynein function
510 reduces the amount of membrane that is added to the arbor over time but does not affect the
511 amount of Ppk1 that is packaged into the membrane destined for dendrites. Thus, interfering
512 with dynein activity perturbs dendrite arborization but does not affect Ppk1 density. Strikingly,
513 even interfering with translation via the knockdown of the ribosomal protein RpL22, which
514 decreases dendrite growth, does not affect dendritic levels of Ppk1. This result is also consistent
515 with the idea that Ppk1 and Ppk channels are packaged into transport packets at a consistent
516 density even if their subsequent transport out of the Golgi is disrupted. Moreover, our analysis of
517 Ppk1::sfGFP levels in dendrite growth mutants, coupled with published reports of Ppk1 or
518 Ppk26 in mutants that affect arbor size, also indicate that Ppk levels typically remain constant or
519 are only minimally affected despite dramatic changes in dendrite arbor size [77–79]. The idea

520 that Ppk1 and Ppk channels are transported to dendrites via the membrane that grows
521 dendrites suggests a mechanism for the coordination of ion channel levels and dendrite arbor
522 size.
523
524 Once Ppk1 reaches the dendrites, our FRAP analysis of membrane-localized Ppk1
525 (Ppk1::GFP(11)^{EC}) suggests that Ppk channels remain stably inserted into the dendritic
526 membrane with little baseline turnover. This idea is also supported by our finding that Ppk1
527 levels are not significantly affected when local protein recycling is disrupted via the expression
528 of Rab5-DN. Moreover, our FRAP analysis of Ppk1::GFP(11)^{EC} did not uncover any hot spots of
529 fluorescent signal recovery that might indicate areas of ion channel addition, although it is
530 possible that such sites of insertion are below our level of detection. Recent qRT-PCR analysis
531 has revealed that Ppk1 mRNA levels drastically decrease after the 2nd instar developmental
532 stage [26], which corresponds to when dendrite growth slows significantly (Parrish et al. 2009).
533 These data, combined with our FRAP results, suggest that Ppk1 is stably integrated into the
534 dendritic membrane as dendrites grow expansively, and, once dendrite growth plateaus, there is
535 little replenishment with newly expressed Ppk1.
536
537 To monitor the membrane localization of Ppk1, we used a novel split-GFP approach. These
538 experiments revealed that Ppk1 is present throughout the somatodendritic membrane but not
539 the membrane of the proximal axon or axon shaft. The clear demarcation of Ppk1::GFP(11)^{EC}
540 fluorescent signal between the somatodendritic and axonal compartments is consistent with the
541 presence of a diffusion barrier between these two compartments in the proximal axon of fly
542 neurons, as was previously supported by studies of the fly ankyrin Ank2 [80–82]. Although there
543 is a barrier to the diffusion of Ppk1 from the somatodendritic membrane to the axonal
544 membrane, Ppk1 is not prevented from being trafficked into the axon to the axon terminal.
545 Given that ensheathing glia likely exclude secGFP(1-10) [36–38], the Ppk1::GFP(11)^{EC}

546 fluorescent signal at axon terminals may reflect the trans-endocytosis of Ppk1 from dendrites to
547 axons. It is not clear what role Ppk1 may play in the axon terminals of class IV da neurons,
548 although other studies, including in flies, support presynaptic roles for Ppk channels and their
549 orthologs [18,19,83]. Additional studies will be needed to determine whether Ppk1 is
550 preferentially trafficked to one compartment or the other and whether Ppk1 may be stably
551 inserted into the dendritic, but not axonal, membrane. Ppk1::GFP(11)^{EC} provides a tool to
552 investigate the spatially restricted membrane expression of Ppk1 and the diffusion barrier
553 between the somatodendritic and axonal membranes.
554
555 Our data indicate that Rab11 plays a role in the transport of Ppk1 to dendrites. Rab11 is an
556 integral component of recycling endosomes but has also been implicated in the anterograde
557 trafficking of receptors and ion channels, including ENaCs, in neuronal and non-neuronal cells
558 [58,59,84–86]. Our results implicate Rab11 in the forward transport of Ppk1 in fly da neurons,
559 which points to the potential conservation of DEG/ENaC/ASIC trafficking pathways across
560 organisms and cell types. Our results indicate that disrupting Rab11 reduces Ppk1 in dendrites
561 but that disrupting the function of Rab5, which acts in early endosomes, does not. This suggests
562 that the effects of perturbing Rab11 on Ppk1 is not due to an effect on Rab11-mediated
563 recycling but is likely due to a disruption of Rab11-mediated forward trafficking of Ppk1 to
564 dendrites. Consistent with this model, Ppk1 levels increase in the cell body when Rab11 levels
565 or function are perturbed. Recently, another group has also found that Ppk26 levels also
566 increase in the cell bodies of neurons with altered Rab11 [28]. It is notable that disrupting Rab11
567 does not lead to a total loss of Ppk1 from dendrites. This may be due to incomplete perturbation
568 of Rab11 or Rab11-positive endosomes, or it could indicate a complementary pathway for the
569 transport of Ppk1 and Ppk channels to dendrites. The pathways that supply membrane and
570 membrane proteins to dendrites, particularly growing dendrites, are still poorly understood. Our

571 data suggest that Rab11 and Rab11-positive endosomes may participate in a pathway that

572 coordinates Ppk ion channel delivery and dendrite arbor expansion.

573 **Materials and Methods**

574

575 **Fly husbandry and stocks**

576 Fruit flies were maintained at 25˚C on cornmeal-molasses-yeast medium. The generation of
577 new *ppk1* alleles and the *UAS-secGFP(1-10)* flies are described below. *ppk26* strains including
578 *ppk26*$^{\Delta 11}$, *UAS-ppk26::mCherry*, and *UAS-ppk26-DEG(A547V)::mCherry* were gifts of Dr. Yuh
579 Nung Jan (UCSF) [21]. The following alleles and transgenic fly strains from the Bloomington
580 Drosophila Stock Center (BDSC), Vienna Drosophila Resource Center (VDRC), and individual
581 laboratories were used: *ppk-Cas9* [57], *Df(3L)BSC673* (BDSC 26525), *ppk-CD4::tdTomato*
582 (BDSC 35845), *ppk-GFP(11)*^{EC}*::CD4::tdTomato* [35], *hsp70-Cre* (BDSC 1092), *DcG-Gal4* [87],
583 *UAS-Dcr-2* (BDSC 24650), *UAS-Dlic-RNAi* (VDRC 41686), *UAS-dynamitin* (BDSC 8784), *UAS-*
584 *EcR-DN* (BDSC 9449), *UAS-GALNT2::TagRFP* (BDSC 65253), *UAS-sfGFP(1-10)* (Bo Huang,
585 UCSF), *UAS-Lva-DN* (BDSC 55055), *nudE*^{39A} [88], *Ppk-Gal4* (BDSC 32078, BDSC 32079),
586 *UASp-Rab5-WT::YFP* (BDSC 24616), *UASp-Rab5-DN[S43N]::YFP* (BDSC 9772), *UAS-*
587 *GFP::Rab5* (BDSC 43336), *UAS-PI3K* (BDSC 8294), *UAS-Rab11-RNAi* (VDRC 108382), *UAS-*
588 *Rab11-DN(3-4)::GFP* (Hsiu-Hsiang Lee, National Taiwan University College of Medicine), *UAS-*
589 *Rac1* (BDSC 6293), *UAS-RpL22 RNAi* (BDSC 34828), *U6-Sec23-gRNA* (BDSC 79400), *w*^{1118}.

590

591 **Generation of *ppk1* alleles**

592 The endogenous *ppk1* gene (~3.7 kb encompassing the entire *ppk1* transcript) was knocked-out
593 and replaced with an attP site to facilitate the reliable integration of new *ppk1* alleles. The
594 *ppk1*$^{attP\text{-}KO}$ strain was generated using CRISPR-Cas9 genome engineering and ends-out gene-
595 targeting [89–91]. We used two guide RNAs that flank *ppk1* (upstream gRNA: 5'-
596 GTTCTTATATCTAGAGATGT-3', and downstream gRNA: 5'-GTCAAGACTTGAAGAATACTG-
597 3') and a donor template, which contained homology arms surrounding an attP site and 3xP3-
598 DsRed flanked by loxP sites. Candidate strains were identified by DsRed expression in adult

599 eyes, and the *ppk1* locus was analyzed by sequencing genomic DNA from isogenized candidate
600 strains. 3xP3-DsRed was then removed by crossing to flies expressing Cre recombinase. A
601 single strain with the desired replacement of *ppk1* with an attP site was used to generate all
602 knock-in alleles.
603
604 Constructs to create knock-in alleles were generated using standard molecular biology
605 techniques and Gibson Assembly to add molecular tags. Two plasmid backbones were used:
606 *pGE-attB-GMR* [90], which includes a *GMR-mini-white*$^{+}$ cassette to identify knock-in alleles by
607 red eye color in adults, and *pBSK-attB-3xP3* (this study), which includes a *3xP3-DsRed*
608 cassette to identify knock-in alleles by DsRed expression in adult eyes. *pBSK-attB-3xP3* was
609 generated by adding an *attB* site and *3xP3-DsRed* to *pBSK*. All the exogenous sequences (e.g.,
610 the product of attB/attP recombination) knocked-into the endogenous *ppk1* locus were the same
611 regardless of which plasmid backbone was used. New *ppk1* alleles in the *pGE-attB-GMR* vector
612 were first subcloned into *pBSK*, modified, and then inserted into *pGE-attB-GMR* using EcoRI
613 and KpnI. New *ppk1* alleles in the *pBSK-attB-3xP3* plasmid were cloned directly using Gibson
614 Assembly (*pBSK-attB-3xP3-ppk*^{WT} was the starting plasmid for many of the knock-in alleles). All
615 constructs were verified by sequencing prior to injection. *attB*-containing plasmids with *ppk1*
616 knock-in alleles were injected into *ppk1*$^{attP\text{-}KO}$ embryos expressing ΦC31 integrase (BestGene
617 Inc., Chino Hills, CA). The *GMR-mini-w*$^{+}$ and *3xP3-DsRed* markers were subsequently removed
618 by crossing to flies expressing Cre recombinase.
619
620 The following alleles were generated in this study: First a wild-type knock-in allele (*ppk1*$^{WT\text{-}k'in}$)
621 was generated by cloning the part of the *ppk1* locus that was eliminated by the replacement
622 strategy (plasmid *pGE-attB-GMR-ppk1*^{WT}*)*. The resulting *ppk1*$^{WT\text{-}K'in}$ flies displayed no overt
623 phenotypes and restored the normal pattern of *ppk1* expression. sfGFP::Ppk1 and Ppk1::sfGFP
624 were created by adding one copy of sfGFP and a GGS(x4) linker at the N- or C-terminus,

625 respectively, of Ppk1 (plasmids *pGE-attB-GMR-sfGFP::ppk1* and *pGE-attB-GMR-ppk1::sfGFP*).
626 A similar approach was used to generate Ppk1::mCherry and sfGFP::Ppk1::mCherry (plasmids
627 *pBSK-attB-3xP3-ppk1::mCherry* and *pBSK-attB-3xP3-sfGFP::ppk1::mCherry*). Ppk1::sfGFP^{EC}-
628 Site 1 and Ppk1::sfGFP^{EC}-Site 2 were created by tagging Ppk1 with one copy of sfGFP at either
629 extracellular Site 1 (between Asn171 and Ile172) or Site 2 (between Gln204 and Leu205).
630 sfGFP was flanked on both sides by a GGS(x4) linker (plasmids *pBSK-attB-3xP3-*
631 *ppk1::sfGFP^{EC}-Site 1* and *pBSK-attB-3xP3-ppk1::sfGFP^{EC}-Site 2)*. Ppk1::GFP(11x3)^{EC} was
632 created by tagging Ppk1 with three copies of the split-GFP peptide GFP(11) at extracellular Site
633 1 (between Asn171 and Ile172). The three copies of GFP(11) were flanked on both sides by a
634 GGS(x4) linker (plasmid *pBSK-attB-3xP3-ppk1::GFP(11x3)^{EC}*). Ppk1::GFP(11x3)^{EC}::mCherry^{C-}
635 ^{term} was created by tagging Ppk1::GFP(11x3)^{EC} at the C-terminus with one copy of mCherry
636 connected by a GGS(x4) linker (plasmid *pBSK-attB-3xP3-ppk1::GFP(11x3)^{EC}::mCherry^{C-term}*).
637 Ppk1::GFP(11x7)$^{C-term}$ was created by tagging Ppk1 with seven copies of GFP(11) at the C-
638 terminus via a GGS(x4) linker (plasmid *pGE-attB-GMR-ppk1::GFP(11x7)*).
639 Ppk1::pHluorin^{EC}::mScarlet^{C-term} and Ppk1::pHluorin^{EC}::mCherry^{C-term} were created by adding one
640 copy of superecliptic pHluorin (synthesized as a gene block by GeneWiz, South Plainfield, NJ)
641 at extracellular Site 1 (between Asn171 and Ile172) and flanked on both sides by a GGS(x4)
642 linker and tagged at the C-terminus with either one copy of mScarlet-I (synthetic gene block
643 from GeneWiz) or one copy of mCherry connected with a GGS(x4) linker (plasmids *pGE-attB-*
644 *GMR-ppk1::pHluorin^{EC}::mScarlet^{C-term}* and *pBSK-attB-3xP3-ppk1::pHluorin^{EC}::mCherry^{C-term}*).
645

646 **Generation of the UAS-secGFP(1-10) transgenic fly strain**

647 The GFP(1-10) coding sequence, which was synthesized as a gBlock fragment (Integrated DNA
648 Technologies, Inc.), was PCR-amplified and cloned into the NheI/XbaI sites of *pIHEU-sfGFP-*
649 *LactC1C2* [92]. The resulting *pIHEU-secGFP(1-10)* construct contains a signal-peptide

650 sequence from Adipokinetic hormone fused in-frame before GFP(1-10). The construct was
651 inserted at the *attP*^{VK00005} site (injected by Rainbow Transgenic Flies, Inc).
652
653 **Fixation and Immunohistochemistry**
654 To visualize Ppk channel expression in larval fillets, wandering third instar larvae were washed
655 in 1X PBS (phosphate buffered saline, pH 7.4), dissected in PHEM buffer (80 mM PIPES pH
656 6.9, 25 mM HEPES pH 7.0, 7 mM $MgCl_2$, 1 mM EGTA) and fixed in 4% paraformaldehyde in 1X
657 PBS with 3.2% sucrose for 20 minutes. For the dissection, larvae were pinned onto a Sylgard
658 plate with their dorsal trachea facing down and were cut on their ventral side to preserve the
659 ddaC neurons. After fixation, the dissected fillets were washed 3 times with 1X PBS, quenched
660 with 50 mM NH_4Cl for 10 minutes, and blocked in blocking buffer composed of 2.5% bovine
661 serum albumin (BSA; catalog number A9647, Sigma), 0.25% fish-skin gelatin (FSG; catalog
662 number G7765, Sigma), 10 mM glycine, and 50 mM NH_4Cl for 3 hours at room temperature.
663 Fillets were incubated in primary antibody diluted in blocking buffer overnight at 4˚C. The next
664 day, fillets were washed in 1X PBS at room temperature (3 x 30 minutes) and incubated with
665 secondary antibody diluted in blocking buffer overnight at 4˚C. The next day, fillets were washed
666 in 1X PBS at room temperature (3 x 30 minutes) and mounted onto glass microscope slides
667 (Fisher Scientific, Selectfrost, 25x75x1.0 mm) with cover glass (Fisher Scientific 24x50-1.5)
668 using elvanol containing antifade (polyvinyl alcohol, Tris-HCl pH 8.5, glycerol and DABCO,
669 catalog number 11247100, Fisher Scientific, Hampton, NH). All wash and incubation steps were
670 performed on a nutator. To visualize membrane levels of Ppk1, a rabbit anti-Ppk1 antibody
671 (1:3000; gift of Yuh Nung Jan, UCSF) [21] targeting an extracellular epitope of Ppk1 was used
672 without detergent in any wash or incubation steps. A fluorescently conjugated secondary
673 antibody was used: goat anti-rabbit-Dylight 633 (1:500; catalog #35563, Invitrogen).
674

675 To visualize Ppk expression in the ventral nerve cord, brains from wandering third instar larvae
676 were isolated from larval carcasses in 1x PBS. Following fixation (4% paraformaldehyde in 1X
677 PBS with 3.2% sucrose for 15 minutes), brains were washed (3 X 5 minutes) in 1x PBS and
678 mounted with the optic lobes facing down. The cover glass was stabilized with four small dots of
679 vacuum grease spacers in four corners of the slide.
680
681 To visualize Ppk1::sfGFP in young ddaC neurons, embryos were collected on grape plates for
682 several hours and then devitalized in a solution of 50% bleach and 50% H_2O for 2-3 minutes.
683 The eggshells were washed away by rinsing with H_2O and then placed in a tube containing
684 equal quantities of n-heptane and fixative (4% paraformaldehyde in 1X PBS) for 10 minutes.
685 Fixed embryos were washed with 1X PBS with 0.1% Triton X-100 (3 x 10 minutes) and then
686 probed for 2 hours with goat anti-HRP conjugated Alexa Fluor 647 (1:1000, or 0.5 mg/mL,
687 Jackson ImmunoResearch, West Grove, PA). The anti-HRP antibody recognizes a glycoprotein
688 epitope that is present throughout the fruit fly nervous system, enabling visualization of virtually
689 all neuronal membranes. Following incubation with the anti-HRP antibody, the embryos were
690 washed in 1X PBS with 0.1% Triton X-100 (3 x 30 minutes). Embryos were mounted in a
691 solution of 50% glycerol and 50% 1X PBS on glass microscope slides (Fisher Scientific,
692 Selectfrost, 25x75x1.0 mm) with cover glass (Global Scientific, 24x50 mm-1.5). All steps were
693 performed at room temperature.
694
695 **Imaging**
696 Imaging was performed on either an SP5 or Stellaris laser-scanning confocal microscope (Leica
697 Microsystems) with sensitive hybrid (HyD) and photomultiplier tube (PMT) detectors using
698 20×0.7 NA (SP5), 20×0.75 NA (Stellaris), and 40×1.3 NA (SP5 and Stellaris) oil-immersion
699 objectives. The dorsal class IV da neurons (ddaCs) in abdominal segments A2-A5 of control
700 and mutant larvae were imaged. For live imaging, individual larvae were placed into a small

701 drop of 50% glycerol:1X PBS solution that was flanked on both sides by strips of vacuum
702 grease spacers. The larva was then immobilized by pressing a cover glass on top of the
703 spacers. The larva was oriented with its dorsal trachea facing up and rolled gently to one side
704 for optimal positioning of the ddaC neurons. Fixed samples (larval fillets, VNCs) were imaged
705 using a 40×1.3 NA oil-immersion objective. Images were collected via z-stacks (1024x1024-
706 pixel resolution, 1 μm per z-step). Movies of Ppk1::sfGFP and Ppk1::mCherry dynamics were
707 collected in 120 h AEL larvae using a 40×1.3 NA oil-immersion objective at a resolution of 1024
708 x 256 pixels, zoom 2.5, and a rate of 2-1.35 frames per second, or 0.5-0.74 seconds per frame,
709 respectively, for a duration of 3 minutes. Movies of Ppk1::GFP(11)^{EC} in growing dendrite tips
710 were collected in 72 h AEL larvae using a 40×1.3 NA oil-immersion objective at a resolution of
711 1024 x 256 pixels, zoom 6, and a rate of 0.34 frames per second (2.942 seconds per frame) for
712 a duration of 3 minutes. For FRAP: First, a pre-bleach z-stack was obtained of the dendrite
713 region to be bleached, which was a secondary dendrite segment longer than 50 μm without
714 branch points, visible in a single z-plane, and within 150 μm of the cell body. A 50 μm circular
715 region of interest (ROI) was centered on the dendrite segment. Next, the Leica FRAP Wizard
716 was used to bleach the ROI: pre-bleach (10 frames; 0.739 sec/frame), bleach at 100% 488 laser
717 intensity (10 frames; 0.739 sec/frame), post-bleach (10 frames; 0.739 sec/frame). After
718 bleaching, z-stacks (z-step size of 0.5 μm) were captured at 1, 3, 5, 10, and 20 minutes post-
719 bleaching. For all experiments, the same imaging settings were used for control and
720 experimental conditions. Images and movies were subsequently analyzed using FIJI or
721 Metamorph.
722
723 **Quantification of Ppk1 signal**
724 Levels of Ppk1 were measured in FIJI using the following reporters: anti-Ppk1 antibody,
725 Ppk1::sfGFP, Ppk1::mCherry, and Ppk1::sfGFP(11x3)^{EC}::mCherry$^{C\text{-}term}$. First, maximum intensity
726 projections of z-stack images were generated. To quantify levels in dendrites, the fluorescence

727 intensity of three different dendrite branches was quantified by tracing 50-μm lines over
728 segments close to the cell body and averaging the signal intensity along each segment. The
729 average intensity of a 50-μm line traced over the background was subtracted from each dendrite
730 trace. Under non-permeabilizing conditions, anti-Ppk1 signal was weak surrounding the cell
731 body, and therefore dendrite traces initiated ~10-15 μm away from the cell body. An average
732 intensity for each neuron was quantified by averaging the intensities of the three dendrite
733 segments after subtracting the background signal. A similar protocol was used to determine the
734 fluorescence intensity of Ppk1::sfGFP in axons: a 50-μm line was traced over the axon close to
735 the cell body and the average intensity of a 50-μm line traced over the background was
736 subtracted.
737
738 To measure the extent of Ppk1::sfGFP signal in growing dendrites over time, z-stack images of
739 Ppk1::sfGFP and CD4::tdTomato taken at two time points 30 sec apart were aligned using the
740 bUnwarpJ plugin to generate a composite image representing the change in dendrite length and
741 fluorescent signal over time. Dendrite length was quantified based on the CD4::tdTomato signal,
742 and the percentage of dendrite that was Ppk1::sfGFP-positive was calculated.
743
744 **Quantification of Ppk1::sfGFP and Ppk1::mCherry dynamics**
745 Movies of Ppk1::sfGFP and Ppk1::mCherry dynamics were first stabilized in FIJI using the
746 Image Stabilizer plugin. Stabilized movies were opened in Metamorph (Molecular Devices, LLC,
747 San Jose, CA), and kymographs were generated by drawing 50-70 μm line segments along
748 dendrites and axons. Frequency was quantified by manually counting the number of motile and
749 stationary puncta (data were normalized to represent the number of puncta in 100 μm and 1
750 minute). To quantify motility, the tracks on each kymograph were manually divided into three
751 categories. Puncta that were motile for the duration of the movie were scored as mobile. Some
752 puncta were both motile and stationary; these puncta were scored as "both." Puncta that did not

753 move (defined as less than 1 μm) for the duration of the 3-minute movie were scored as
754 stationary. To quantify directionality, the tracks on the kymograph were manually scored as
755 anterograde (away from the cell body), retrograde (towards the cell body), or bidirectional
756 (anterograde and retrograde movement). To quantify velocity, tracks on the kymograph were
757 traced, and the corresponding data on time and distance were exported to Excel to calculate
758 velocity.
759
760 **Quantification of dendrite morphology**
761 Imaris software with Filament Tracer (version 9.7-9.8, Oxford Instruments) was used to quantify
762 dendrite length and the number of terminal tips. Neurons were analyzed in larvae that were
763 aged to 72 h AEL unless otherwise mentioned. To capture the entire ddaC dendritic arbor, z-
764 stacks (1024x1024-pixel resolution, 1 μm per z-step) of neurons expressing fluorescent
765 membrane markers were captured using a 20×0.7 NA (Leica SP5) 20×0.75 NA (Leica Stellaris)
766 oil-immersion objectives. Maximum intensity projections of the z-stack images were created in
767 FIJI, and neighboring neurons were cropped out using the freehand draw tool. These images
768 were then further processed in FIJI by applying a threshold to eliminate background signal. The
769 images were imported into Imaris, and Filament Tracer (BitPlane) with automatic detection was
770 used to quantify total dendrite length and the number of terminal tips. The largest and smallest
771 diameters of each neuron were manually measured to generate the dendrite start points and
772 seed points. The thresholds were manually adjusted for the start points and seed points in order
773 to cover the entire arbor and to reduce background points; seed points were manually added to
774 segments that were not automatically identified. The filament was edited to remove the axon
775 segment and to correct misdrawn segments. Measurements generated in Imaris were exported
776 to Excel for further analysis.
777
778 **Quantification of FRAP**

Analysis was performed in FIJI by creating maximum projections of the z-stacks from each time point. A line trace through the bleached region was drawn and the average intensity (arbitrary units; AU) of the center 10 μm was used to quantify the signal recovery over time. To account for general photobleaching, the signal intensity in the bleached 10 μm section was normalized by dividing by the average intensity (AU) of a 10 μm segment in a different secondary branch outside of the bleached region. Average intensity values were exported to Excel for further analysis. To calculate percent recovery of signal after photobleaching, the normalized average signal of the 10 μm branched region at 1, 3, 5, 10, and 20 minutes was divided by the initial signal from the pre-bleach z-stack.

Statistical Analysis

All data were blinded prior to analysis. Statistical analysis was performed in Excel and GraphPad Prism using a significance level of $p < 0.05$. Outliers were identified using Grubbs' test and removed. Data were analyzed for normality using the Shapiro-Wilk test. Normally distributed data were then analyzed for equal variance and significance using either an F-test and Student's unpaired t-test (two samples) or one-way ANOVA with post-hoc Tukey (multiple samples). Data sets that were not normally distributed were analyzed using Mann-Whitney U test (two samples) or Kruskal-Wallis test with post-hoc Dunn test for significance (multiple samples). Significance levels are represented as follows: not significant (ns), $p > 0.05$; *, $p = 0.05$-0.01; **, $p = 0.01$-0.001; ***, $p = 0.001$-0.0001; and ****, $p < 0.0001$. Data are presented as the mean ± standard error of the mean (SEM) unless otherwise noted. In the graphs, *n* represents a neuron unless otherwise indicated.

Acknowledgements

We thank Drs. Yuh Nung Jan (University of California, San Francisco), Hsiu-Hsiang Lee (National Taiwan University College of Medicine), Bing Ye (University of Michigan), the Bloomington Drosophila Stock Center (NIH P40OD018537), and the Vienna Drosophila Resource Center for fly strains and antibodies. We thank Dr. Anjon Audhya and Jennifer Peotter (University of Wisconsin-Madison) for assistance with the Imaris software. We thank members of the Wildonger lab for their feedback and suggestions on the project and manuscript; in particular, we thank Jessica Liang for her contributions to developing the FRAP protocol, Dena Johnson-Schlitz for technical assistance and advice, and Harriet Saunders for helpful guidance. We thank the Biochemistry Department and Dr. Aaron Hoskins (University of Wisconsin-Madison) for generously supporting J.M..

Competing interests: The authors have declared that no competing interests exist.

Author Contributions

Conceptualization: Josephine W. Mitchell and Jill Wildonger

Formal analysis: Josephine W. Mitchell and Ipek Midillioglu

Funding acquisition: Chun Han and Jill Wildonger

Investigation: Josephine W. Mitchell and Ipek Midillioglu

Resources: Bei Wang and Chun Han

Project administration: Chun Han and Jill Wildonger

Supervision: Jill Wildonger

Visualization: Josephine W. Mitchell

Writing – original draft: Josephine W. Mitchell and Jill Wildonger

Writing – review & editing: Josephine W. Mitchell, Ipek Midillioglu, Bei Wang, Chun Han, and Jill Wildonger

827 **References**

828

829 1. Bourke AM, Bowen AB, Kennedy MJ. New approaches for solving old problems in neuronal
830 protein trafficking. Mol Cell Neurosci. 2018. doi:10.1016/j.mcn.2018.04.004

831 2. Grueber WB, Jan LY, Jan YN. Tiling of the Drosophila epidermis by multidendritic sensory
832 neurons. Dev Camb Engl. 2002;129: 2867–78.

833 3. Tracey WD, Wilson RI, Laurent G, Benzer S. painless, a Drosophila Gene Essential for
834 Nociception. Cell. 2003;113: 261–273. doi:10.1016/s0092-8674(03)00272-1

835 4. Xiang Y, Yuan Q, Vogt N, Looger LL, Jan LY, Jan YN. Light-avoidance-mediating
836 photoreceptors tile the Drosophila larval body wall. Nature. 2010;468: 921–926.
837 doi:10.1038/nature09576

838 5. Hwang RY, Zhong L, Xu Y, Johnson T, Zhang F, Deisseroth K, et al. Nociceptive Neurons
839 Protect Drosophila Larvae from Parasitoid Wasps. Curr Biol. 2007;17: 2105–2116.
840 doi:10.1016/j.cub.2007.11.029

841 6. Parrish JZ, Xu P, Kim CC, Jan LY, Jan YN. The microRNA bantam Functions in Epithelial
842 Cells to Regulate Scaling Growth of Dendrite Arbors in Drosophila Sensory Neurons. Neuron.
843 2009;63: 788–802. doi:10.1016/j.neuron.2009.08.006

844 7. Grueber WB, Ye B, Moore AW, Jan LY, Jan YN. Dendrites of Distinct Classes of Drosophila
845 Sensory Neurons Show Different Capacities for Homotypic Repulsion. Curr Biol. 2003;13: 618–
846 626. doi:10.1016/s0960-9822(03)00207-0

847 8. Jan Y-N, Jan LY. Branching out: mechanisms of dendritic arborization. Nat Rev Neurosci.
848 2010;11: 316–328. doi:10.1038/nrn2836

849 9. Singhania A, Grueber WB. Development of the embryonic and larval peripheral nervous
850 system of Drosophila. Wiley Interdiscip Rev Dev Biology. 2014;3: 193–210.
851 doi:10.1002/wdev.135

852 10. Hall DH, Treinin M. How does morphology relate to function in sensory arbors? Trends
853 Neurosci. 2011;34: 443–451. doi:10.1016/j.tins.2011.07.004

854 11. Lumpkin EA, Caterina MJ. Mechanisms of sensory transduction in the skin. Nature.
855 2007;445: 858–865. doi:10.1038/nature05662

856 12. He J, Li B, Han S, Zhang Y, Liu K, Yi S, et al. Drosophila as a Model to Study the
857 Mechanism of Nociception. Front Physiol. 2022;13: 854124. doi:10.3389/fphys.2022.854124

858 13. Coste B, Xiao B, Santos JS, Syeda R, Grandl J, Spencer KS, et al. Piezos are pore-forming
859 subunits of mechanically activated channels. Nature. 2012;483: 176–181.
860 doi:10.1038/nature10812

861 14. Kim SE, Coste B, Chadha A, Cook B, Patapoutian A. The role of Drosophila Piezo in
862 mechanical nociception. Nature. 2012;483: 209. doi:10.1038/nature10801

863 15. Zhong L, Hwang RY, Tracey WD. Pickpocket Is a DEG/ENaC Protein Required for
864 Mechanical Nociception in Drosophila Larvae. Curr Biol. 2010;20: 429–434.
865 doi:10.1016/j.cub.2009.12.057

866 16. Adams CM, Anderson MG, Motto DG, Price MP, Johnson WA, Welsh MJ. Ripped Pocket
867 and Pickpocket, Novel Drosophila DEG/ENaC Subunits Expressed in Early Development and in
868 Mechanosensory Neurons. J Cell Biology. 1998;140: 143–152. doi:10.1083/jcb.140.1.143

869 17. Jasti J, Furukawa H, Gonzales EB, Gouaux E. Structure of acid-sensing ion channel 1 at 1.9
870 Å resolution and low pH. Nature. 2007;449: 316–323. doi:10.1038/nature06163

871 18. Bianchi L. Ion Channels in Biophysics and Physiology. Adv Exp Med Biol. 2022;1349: 165–
872 192. doi:10.1007/978-981-16-4254-8_9

873 19. Kellenberger S, Schild L. Epithelial Sodium Channel/Degenerin Family of Ion Channels: A
874 Variety of Functions for a Shared Structure. Physiol Rev. 2002;82: 735–767.
875 doi:10.1152/physrev.00007.2002

876 20. Boscardin E, Alijevic O, Hummler E, Frateschi S, Kellenberger S. The function and
877 regulation of acid-sensing ion channels (ASICs) and the epithelial Na+ channel (ENaC):
878 IUPHAR Review 19. Brit J Pharmacol. 2016;173: 2671–2701. doi:10.1111/bph.13533

879 21. Gorczyca DA, Younger S, Meltzer S, Kim SE, Cheng L, Song W, et al. Identification of
880 Ppk26, a DEG/ENaC Channel Functioning with Ppk1 in a Mutually Dependent Manner to Guide
881 Locomotion Behavior in Drosophila. Cell Reports. 2014;9: 1446–1458.
882 doi:10.1016/j.celrep.2014.10.034

883 22. Guo Y, Wang Y, Wang Q, Wang Z. The Role of PPK26 in Drosophila Larval Mechanical
884 Nociception. Cell Reports. 2014;9: 1183–1190. doi:10.1016/j.celrep.2014.10.020

885 23. Mauthner SE, Hwang RY, Lewis AH, Xiao Q, Tsubouchi A, Wang Y, et al. Balboa Binds to
886 Pickpocket In Vivo and Is Required for Mechanical Nociception in Drosophila Larvae. Curr Biol.
887 2014;24: 2920–2925. doi:10.1016/j.cub.2014.10.038

888 24. Zelle KM, Lu B, Pyfrom SC, Ben-Shahar Y. The Genetic Architecture of Degenerin/Epithelial
889 Sodium Channels in Drosophila. G3 Genes Genomes Genetics. 2013;3: 441–450.
890 doi:10.1534/g3.112.005272

891 25. Darboux I, Lingueglia E, Pauron D, Barbry P, Lazdunski M. A New Member of the Amiloride-
892 Sensitive Sodium Channel Family inDrosophila melanogasterPeripheral Nervous System.
893 Biochem Bioph Res Co. 1998;246: 210–216. doi:10.1006/bbrc.1998.8183

894 26. Jaszczak JS, DeVault L, Jan LY, Jan YN. Steroid hormone signaling activates thermal
895 nociception during Drosophila peripheral nervous system development. Elife. 2022;11: e76464.
896 doi:10.7554/elife.76464

897 27. Ainsley JA, Kim MJ, Wegman LJ, Pettus JM, Johnson WA. Sensory mechanisms controlling
898 the timing of larval developmental and behavioral transitions require the Drosophila DEG/ENaC
899 subunit, Pickpocket1. Dev Biol. 2008;322: 46–55. doi:10.1016/j.ydbio.2008.07.003

900 28. Krämer R, Rode S, Rumpf S. Rab11 is required for neurite pruning and developmental
901 membrane protein degradation in Drosophila sensory neurons. Dev Biol. 2019;451: 68–78.
902 doi:10.1016/j.ydbio.2019.03.003

903 29. Chudakov DM, Matz MV, Lukyanov S, Lukyanov KA. Fluorescent Proteins and Their
904 Applications in Imaging Living Cells and Tissues. Physiol Rev. 2010;90: 1103–1163.
905 doi:10.1152/physrev.00038.2009

906 30. Couturier L, Trylinski M, Mazouni K, Darnet L, Schweisguth F. A fluorescent tagging
907 approach in Drosophila reveals late endosomal trafficking of Notch and Sanpodo. J Cell Biol.
908 2014;207: 351–363. doi:10.1083/jcb.201407071

909 31. Miesenböck G, Angelis DAD, Rothman JE. Visualizing secretion and synaptic transmission
910 with pH-sensitive green fluorescent proteins. Nature. 1998;394: 192–195. doi:10.1038/28190

911 32. Chen X, Gründer S. Permeating protons contribute to tachyphylaxis of the acid-sensing ion
912 channel (ASIC) 1a. J Physiology. 2007;579: 657–670. doi:10.1113/jphysiol.2006.120733

913 33. Kamiyama R, Banzai K, Liu P, Marar A, Tamura R, Jiang F, et al. Cell-type–specific,
914 multicolor labeling of endogenous proteins with split fluorescent protein tags in Drosophila. Proc
915 National Acad Sci. 2021;118: e2024690118. doi:10.1073/pnas.2024690118

916 34. Ji H, Sapar ML, Sarkar A, Wang B, Han C. Phagocytosis and self-destruction break down
917 dendrites of Drosophila sensory neurons at distinct steps of Wallerian degeneration. P Natl
918 Acad Sci Usa. 2022;119: e2111818119. doi:10.1073/pnas.2111818119

919 35. Han C, Wang D, Soba P, Zhu S, Lin X, Jan LY, et al. Integrins Regulate Repulsion-Mediated
920 Dendritic Patterning of Drosophila Sensory Neurons by Restricting Dendrites in a 2D Space.
921 Neuron. 2012;73: 64–78. doi:10.1016/j.neuron.2011.10.036

922 36. Banerjee S. Axonal Ensheathment and Septate Junction Formation in the Peripheral
923 Nervous System of Drosophila. J Neurosci. 2006;26: 3319–3329. doi:10.1523/jneurosci.5383-
924 05.2006

925 37. Freeman MR. Drosophila Central Nervous System Glia. Csh Perspect Biol. 2015;7:
926 a020552. doi:10.1101/cshperspect.a020552

927 38. Stork T, Engelen D, Krudewig A, Silies M, Bainton RJ, Klambt C. Organization and Function
928 of the Blood Brain Barrier in Drosophila. J Neurosci. 2008;28: 587–597.
929 doi:10.1523/jneurosci.4367-07.2008

930 39. Bianchi L, Gerstbrein B, Frøkjær-Jensen C, Royal DC, Mukherjee G, Royal MA, et al. The
931 neurotoxic MEC-4(d) DEG/ENaC sodium channel conducts calcium: implications for necrosis
932 initiation. Nat Neurosci. 2004;7: 1337–1344. doi:10.1038/nn1347

933 40. Brown AL, Fernandez-Illescas SM, Liao Z, Goodman MB. Gain-of-Function Mutations in the
934 MEC-4 DEG/ENaC Sensory Mechanotransduction Channel Alter Gating and Drug Blockade. J
935 Gen Physiology. 2007;129: 161–173. doi:10.1085/jgp.200609672

936 41. Lin W-Y, Williams C, Yan C, Koledachkina T, Luedke K, Dalton J, et al. The SLC36
937 transporter Pathetic is required for extreme dendrite growth in Drosophila sensory neurons.
938 Gene Dev. 2015;29: 1120–1135. doi:10.1101/gad.259119.115

939 42. Ou Y, Chwalla B, Landgraf M, Meyel DJ van. Identification of genes influencing dendrite
940 morphogenesis in developing peripheral sensory and central motor neurons. Neural Dev.
941 2008;3: 16. doi:10.1186/1749-8104-3-16

942 43. Emoto K, He Y, Ye B, Grueber WB, Adler PN, Jan LY, et al. Control of Dendritic Branching
943 and Tiling by the Tricornered-Kinase/Furry Signaling Pathway in Drosophila Sensory Neurons.
944 Cell. 2004;119: 245–256. doi:10.1016/j.cell.2004.09.036

945 44. Rolls MM. Neuronal polarity in Drosophila: Sorting out axons and dendrites. Dev Neurobiol.
946 2011;71: 419–429. doi:10.1002/dneu.20836

947 45. Zheng Y, Wildonger J, Ye B, Zhang Y, Kita A, Younger SH, et al. Dynein is required for
948 polarized dendritic transport and uniform microtubule orientation in axons. Nat Cell Biol.
949 2008;10: 1172–1180. doi:10.1038/ncb1777

950 46. Satoh D, Sato D, Tsuyama T, Saito M, Ohkura H, Rolls MM, et al. Spatial control of
951 branching within dendritic arbors by dynein-dependent transport of Rab5-endosomes. Nat Cell
952 Biol. 2008;10: 1164–1171. doi:10.1038/ncb1776

953 47. Arthur AL, Yang SZ, Abellaneda AM, Wildonger J. Dendrite arborization requires the dynein
954 cofactor NudE. J Cell Sci. 2015;128: 2191–2201. doi:10.1242/jcs.170316

955 48. Echeverri CJ, Paschal BM, Vaughan KT, Vallee RB. Molecular characterization of the 50-kD
956 subunit of dynactin reveals function for the complex in chromosome alignment and spindle
957 organization during mitosis. J Cell Biology. 1996;132: 617–633. doi:10.1083/jcb.132.4.617

958 49. Schroer TA. DYNACTIN. Annu Rev Cell Dev Bi. 2004;20: 759–779.
959 doi:10.1146/annurev.cellbio.20.012103.094623

960 50. Gardiol A, Racca C, Triller A. Dendritic and Postsynaptic Protein Synthetic Machinery. J
961 Neurosci. 1999;19: 168–179. doi:10.1523/jneurosci.19-01-00168.1999

962 51. Horton AC, Ehlers MD. Dual Modes of Endoplasmic Reticulum-to-Golgi Transport in
963 Dendrites Revealed by Live-Cell Imaging. J Neurosci. 2003;23: 6188–6199.
964 doi:10.1523/jneurosci.23-15-06188.2003

965 52. Ye B, Zhang Y, Song W, Younger SH, Jan LY, Jan YN. Growing Dendrites and Axons Differ
966 in Their Reliance on the Secretory Pathway. Cell. 2007;130: 717–729.
967 doi:10.1016/j.cell.2007.06.032

968 53. Zhou W, Chang J, Wang X, Savelieff MG, Zhao Y, Ke S, et al. GM130 Is Required for
969 Compartmental Organization of Dendritic Golgi Outposts. Curr Biol. 2014;24: 1227–1233.
970 doi:10.1016/j.cub.2014.04.008

971 54. Yang SZ, Wildonger J. Golgi Outposts Locally Regulate Microtubule Orientation in Neurons
972 but Are Not Required for the Overall Polarity of the Dendritic Cytoskeleton. Genetics. 2020;215:
973 genetics.302979.2019. doi:10.1534/genetics.119.302979

974 55. Papoulas O, Hays TS, Sisson JC. The golgin Lava lamp mediates dynein-based Golgi
975 movements during Drosophila cellularization. Nat Cell Biol. 2004;7: 612–618.
976 doi:10.1038/ncb1264

977 56. Sisson JC, Field C, Ventura R, Royou A, Sullivan W. Lava Lamp, a Novel Peripheral Golgi
978 Protein, Is Required for Drosophila melanogaster Cellularization. J Cell Biology. 2000;151: 905–
979 918. doi:10.1083/jcb.151.4.905

980 57. Poe AR, Wang B, Sapar ML, Ji H, Li K, Onabajo T, et al. Robust CRISPR/Cas9-Mediated
981 Tissue Specific Mutagenesis Reveals Gene Redundancy and Perdurance in Drosophila.
982 Genetics. 2018;211: genetics.301736.2018. doi:10.1534/genetics.118.301736

983 58. Bowen AB, Bourke AM, Hiester BG, Hanus C, Kennedy MJ. Golgi-independent secretory
984 trafficking through recycling endosomes in neuronal dendrites and spines. Elife. 2017;6:
985 e27362. doi:10.7554/elife.27362

986 59. Ware AW, Rasulov SR, Cheung TT, Lott JS, McDonald FJ. Membrane trafficking pathways
987 regulating the epithelial Na+ channel. Am J Physiol-renal. 2020;318: F1–F13.
988 doi:10.1152/ajprenal.00277.2019

989 60. Karpushev AV, Levchenko V, Pavlov TS, Lam V, Vinnakota KC, Vandewalle A, et al.
990 Regulation of ENaC expression at the cell surface by Rab11. Biochem Bioph Res Co. 2008;377:
991 521–525. doi:10.1016/j.bbrc.2008.10.014

992 61. Butterworth MB, Edinger RS, Silvis MR, Gallo LI, Liang X, Apodaca G, et al. Rab11b
993 regulates the trafficking and recycling of the epithelial sodium channel (ENaC). Am J Physiol-
994 renal. 2012;302: F581–F590. doi:10.1152/ajprenal.00304.2011

995 62. Lin T, Kao H-H, Chou C-H, Chou C-Y, Liao Y-C, Lee H-H. Rab11 activation by Ik2 kinase is
996 required for dendrite pruning in Drosophila sensory neurons. Plos Genet. 2020;16: e1008626.
997 doi:10.1371/journal.pgen.1008626

998 63. Hausser A, Schlett K. Coordination of AMPA receptor trafficking by Rab GTPases. Small
999 Gtpases. 2017;10: 419–432. doi:10.1080/21541248.2017.1337546

1000 64. Zhang J, Schulze KL, Hiesinger PR, Suyama K, Wang S, Fish M, et al. Thirty-One Flavors
1001 of Drosophila Rab Proteins. Genetics. 2007;176: 1307–1322. doi:10.1534/genetics.106.066761

1002 65. Kerstein PC, Nichol RH, Gomez TM. Mechanochemical regulation of growth cone motility.
1003 Front Cell Neurosci. 2015;9: 244. doi:10.3389/fncel.2015.00244

1004 66. Liu X, Liu C, Ye J, Zhang S, Wang K, Su R. Distribution of Acid Sensing Ion Channels in
1005 Axonal Growth Cones and Presynaptic Membrane of Cultured Hippocampal Neurons. Front Cell
1006 Neurosci. 2020;14: 205. doi:10.3389/fncel.2020.00205

1007 67. Wang PY, Petralia RS, Wang Y-X, Wenthold RJ, Brenowitz SD. Functional NMDA
1008 Receptors at Axonal Growth Cones of Young Hippocampal Neurons. J Neurosci. 2011;31:
1009 9289–9297. doi:10.1523/jneurosci.5639-10.2011

1010 68. Gill I, Droubi S, Giovedi S, Fedder KN, Bury LAD, Bosco F, et al. Presynaptic NMDA
1011 receptors – dynamics and distribution in developing axons in vitro and in vivo. J Cell Sci.
1012 2014;128: 768–780. doi:10.1242/jcs.162362

1013 69. Schenk U, Verderio C, Benfenati F, Matteoli M. Regulated delivery of AMPA receptor
1014 subunits to the presynaptic membrane. Embo J. 2003;22: 558–568. doi:10.1093/emboj/cdg059

1015 70. Herkert M, Röttger S, Becker C. The NMDA receptor subunit NR2B of neonatal rat brain:
1016 complex formation and enrichment in axonal growth cones. Eur J Neurosci. 1998;10: 1553–
1017 1562. doi:10.1046/j.1460-9568.1998.00164.x

1018 71. Ehlers MD, Fung ET, O'Brien RJ, Huganir RL. Splice Variant-Specific Interaction of the
1019 NMDA Receptor Subunit NR1 with Neuronal Intermediate Filaments. J Neurosci. 1998;18: 720–
1020 730. doi:10.1523/jneurosci.18-02-00720.1998

1021 72. Tao L, Coakley S, Shi R, Shen K. Dendrites use mechanosensitive channels to proofread
1022 ligand-mediated guidance during morphogenesis. Biorxiv. 2022; 2022.02.28.482179.
1023 doi:10.1101/2022.02.28.482179

1024 73. Honjo K, Mauthner SE, Wang Y, Skene JHP, Tracey WD. Nociceptor-Enriched Genes
1025 Required for Normal Thermal Nociception. Cell Reports. 2016;16: 295–303.
1026 doi:10.1016/j.celrep.2016.06.003

1027 74. Wong ROL, Ghosh A. Activity-dependent regulation of dendritic growth and patterning. Nat
1028 Rev Neurosci. 2002;3: 803–812. doi:10.1038/nrn941

1029 75. Rao A, Kim E, Sheng M, Craig AM. Heterogeneity in the Molecular Composition of
1030 Excitatory Postsynaptic Sites during Development of Hippocampal Neurons in Culture. J
1031 Neurosci. 1998;18: 1217–1229. doi:10.1523/jneurosci.18-04-01217.1998

1032 76. Craig AM, Blackstone CD, Huganir RL, Banker G. The distribution of glutamate receptors in
1033 cultured rat hippocampal neurons: Postsynaptic clustering of AMPA selective subunits. Neuron.
1034 1993;10: 1055–1068. doi:10.1016/0896-6273(93)90054-u

1035 77. Ziegler AB, Thiele C, Tenedini F, Richard M, Leyendecker P, Hoermann A, et al. Cell-
1036 Autonomous Control of Neuronal Dendrite Expansion via the Fatty Acid Synthesis Regulator
1037 SREBP. Cell Reports. 2017;21: 3346–3353. doi:10.1016/j.celrep.2017.11.069

1038 78. Hu C, Kanellopoulos AK, Richter M, Petersen M, Konietzny A, Tenedini F, et al. Conserved
1039 Tao kinase activity regulates dendritic arborization, cytoskeletal dynamics and sensory function

1040 in Drosophila. J Neurosci Official J Soc Neurosci. 2020; 1846–19. doi:10.1523/jneurosci.1846-
1041 19.2020

1042 79. Rui M, Bu S, Chew LY, Wang Q, Yu F. The membrane protein Raw regulates dendrite
1043 pruning via the secretory pathway. Development. 2020;147: dev191155.
1044 doi:10.1242/dev.191155

1045 80. Jegla T, Nguyen MM, Feng C, Goetschius DJ, Luna E, Rossum DB van, et al. Bilaterian
1046 Giant Ankyrins Have a Common Evolutionary Origin and Play a Conserved Role in Patterning
1047 the Axon Initial Segment. Plos Genet. 2016;12: e1006457. doi:10.1371/journal.pgen.1006457

1048 81. Winckler B, Forscher P, Mellman I. A diffusion barrier maintains distribution of membrane
1049 proteins in polarized neurons. Nature. 1999;397: 698–701. doi:10.1038/17806

1050 82. Leterrier C. The Axon Initial Segment: An Updated Viewpoint. J Neurosci. 2018;38: 2135–
1051 2145. doi:10.1523/jneurosci.1922-17.2018

1052 83. Younger MA, Müller M, Tong A, Pym EC, Davis GW. A Presynaptic ENaC Channel Drives
1053 Homeostatic Plasticity. Neuron. 2013;79: 1183–1196. doi:10.1016/j.neuron.2013.06.048

1054 84. Lock JG, Stow JL. Rab11 in Recycling Endosomes Regulates the Sorting and Basolateral
1055 Transport of E-Cadherin. Mol Biol Cell. 2005;16: 1744–1755. doi:10.1091/mbc.e04-10-0867

1056 85. Cresawn KO, Potter BA, Oztan A, Guerriero CJ, Ihrke G, Goldenring JR, et al. Differential
1057 involvement of endocytic compartments in the biosynthetic traffic of apical proteins. Embo J.
1058 2007;26: 3737–3748. doi:10.1038/sj.emboj.7601813

1059 86. Ang AL, Taguchi T, Francis S, Fölsch H, Murrells LJ, Pypaert M, et al. Recycling
1060 endosomes can serve as intermediates during transport from the Golgi to the plasma
1061 membrane of MDCK cells. J Cell Biology. 2004;167: 531–543. doi:10.1083/jcb.200408165

1062 87. Suh JM, Gao X, McKay J, McKay R, Salo Z, Graff JM. Hedgehog signaling plays a
1063 conserved role in inhibiting fat formation. Cell Metab. 2006;3: 25–34.
1064 doi:10.1016/j.cmet.2005.11.012

1065 88. Wainman A, Creque J, Williams B, Williams EV, Bonaccorsi S, Gatti M, et al. Roles of the
1066 Drosophila NudE protein in kinetochore function and centrosome migration. J Cell Sci.
1067 2009;122: 1747–1758. doi:10.1242/jcs.041798

1068 89. Gratz SJ, Cummings AM, Nguyen JN, Hamm DC, Donohue LK, Harrison MM, et al.
1069 Genome Engineering of Drosophila with the CRISPR RNA-Guided Cas9 Nuclease. Genetics.
1070 2013;194: 1029–1035. doi:10.1534/genetics.113.152710

1071 90. Huang J, Zhou W, Dong W, Watson AM, Hong Y. Directed, efficient, and versatile
1072 modifications of the Drosophila genome by genomic engineering. Proc Natl Acad Sci. 2009;106:
1073 8284–8289. doi:10.1073/pnas.0900641106

1074 91. Huang J, Zhou W, Watson AM, Jan Y-N, Hong Y. Efficient Ends-Out Gene Targeting In
1075 Drosophila. Genetics. 2008;180: 703–707. doi:10.1534/genetics.108.090563

1076 92. Sapar ML, Ji H, Wang B, Poe AR, Dubey K, Ren X, et al. Phosphatidylserine Externalization
1077 Results from and Causes Neurite Degeneration in Drosophila. Cell Reports. 2018;24: 2273–
1078 2286. doi:10.1016/j.celrep.2018.07.095

1079

1080

1081 **Figure Legends**

1082

1083 **Fig 1. Endogenously tagged Ppk1 is enriched in dendrites but also localizes to axons.**
1084 Images of ddaC neurons and their axon terminals in live 3rd instar larvae (B, D-F) and fixed
1085 ventral nerve cords (VNCs) (C, F). Dashed-outline boxes: Individual 1-μm thick z-plane zoomed-
1086 in views of dendrites and axons; a line indicates the position at which an intensity profile plot
1087 was generated (B, D). (A) Cartoon illustrating the CRISPR-Cas9-engineered *ppk1* locus in
1088 which endogenous *ppk1* was replaced with an attP "docking" site for reliable, rapid knock-in of
1089 new *ppk1* alleles. (B, C) Representative images of Ppk1::sfGFP in the cell body, dendrites, and
1090 axon (B) and axon terminals in the VNC (C). CD4::tdTomato marks the axon terminals of the
1091 class IV neurons in the VNC (C). Scale bars, 50 μm (B), 10 μm (C), and 5 μm (dashed-outline
1092 boxes, B). (D) Representative image of Ppk1::mCherry. Scale bars, 50 μm and 5 μm (dashed-
1093 outline boxes). (E) Representative kymographs and quantification of Ppk1::mCherry puncta in
1094 dendrites and axons. Quantification, Ppk1::mCherry puncta density: Mann-Whitney test
1095 ($p<0.0001$); dendrites (16 dendrite segments, 12 larvae) v. axons (12 axon segments, 9 larvae).
1096 In the graph, each data point represents a dendrite or axon segment. Quantification,
1097 Ppk1::mCherry puncta motility and directionality: dendrites (16 dendrite segments, 12 larvae)
1098 and axons (12 axon segments, 9 larvae). Quantification, Ppk1::mCherry puncta velocity:
1099 Student's unpaired t-test ($p=0.8786$); dendrites (15 dendrite segments, 11 larvae) v. axons (12
1100 axon segments, 9 larvae). In the graph, each data point represents the average velocity of
1101 Ppk1::mCherry puncta in a dendrite or axon segment. Data are plotted as mean ± SEM.
1102 n.s.=not significant ($p>0.05$) and ****$p<0.0001$. (F) Representative images of dual-tagged
1103 sfGFP::Ppk1::mCherry in dendrites, cell body and axon (top and middle), and axon terminal in
1104 the VNC (bottom). Scale bars, 50 μm (top), 5 μm (middle), 10 μm (bottom). (G) Representative
1105 images of the cell body and proximal dendrites of Ppk1::sfGFP, Ppk1::mCherry, and
1106 sfGFP::Ppk1::mCherry. Scale bar, 10 μm.

1107 **Fig 2. Membrane localization of Ppk1 visualized in live larvae with the secreted split-GFP**
1108 **system.**
1109 Images of ddaC neurons in live 3rd instar larvae (B-D) and fixed ventral nerve cords (VNCs) (E).
1110 Dashed-outline boxes: zoomed-in views of dendrite branches (B, C) and cell bodies (D) from the
1111 control neuron shown in panel B. (A) Cartoon of secreted-split-GFP approach to label Ppk1
1112 when it is inserted into the neuronal membrane. Secreted GFP(1-10) (secGFP(1-10)) is
1113 expressed by the fat bodies, which secrete secGFP(1-10) into the hemolymph that circulates
1114 throughout the larva. When secGFP(1-10) encounters and binds GFP(11) incorporated into an
1115 extracellular loop of ppk1, GFP is reconstituted and fluoresces. (B-D) Representative images of
1116 GFP and mCherry fluorescence in neurons expressing either Ppk1 dual-tagged with 3 copies of
1117 GFP(11) extracellularly (EC) and mCherry at the C-terminus (Ppk1::GFP(11x3)^{EC}::mCherry$^{C\text{-}term}$)
1118 (B-D) or a control construct comprised of the single-pass transmembrane protein CD4 tagged
1119 extracellularly with one copy of GFP(11) and intracellularly with tdTomato
1120 (GFP(11)^{EC}::CD4::tdTomato) (D). UAS-secGFP(1-10) expression was driven in the fat bodies by
1121 DcG-Gal4. GFP fluorescence reveals that ppk1 is present in the neuronal membrane of the
1122 dendrites (B, C) and cell body (B, D) but not the axon, even though mCherry reveals that Ppk1
1123 is present in axons (B, D). In contrast, GFP(11)^{EC}::CD4::tdTomato displays reconstituted GFP
1124 signal in both the cell body and the axon (D). Loss of *ppk26* (Δppk26: *ppk26*$^{\Delta 11/\Delta 11}$) results in an
1125 absence of GFP fluorescence from Ppk1::GFP(11x3)^{EC}::mCherry$^{C\text{-}term}$ (B). Panel C shows a
1126 single 1-μm thick z-plane image of a dendrite segment from the neuron in panel B; the line
1127 indicates the position at which the intensity profile plot was generated. AU: arbitrary units. Solid
1128 arrowheads: cell body (B); open arrowheads: cell body-axon boundary (D). Scale bars, 50 μm
1129 (B, solid-outline boxes), 10 μm (B, dashed-outline boxes; D), and 5 μm (C). (E) Representative
1130 images of Ppk1::GFP(11x3)^{EC}::mCherry$^{C\text{-}term}$ in axon terminals in the VNC. Scale bars, 10 μm.
1131 Solid arrowheads: mCherry signal in the axons terminating in the VNC.
1132

1133 **Fig 3. Ppk1 is present in actively growing dendrites but the Pickpocket channel is not**
1134 **required for dendrite growth.**
1135 Images of ddaC neurons in fixed embryos (A) and live 3rd instar larvae (B-E). (A) Ppk1::sfGFP in
1136 the cell body and axon of a ddaC neuron in a late-stage embryo. The ddaC neuron is part of a
1137 cluster of sensory neurons, which are marked by anti-HRP. Arrowheads point to Ppk1::sfGFP in
1138 nascent dendrites. Scale bar, 10 μm. (B) Quantification of the distribution of Ppk1::sfGFP in
1139 growing dendrite branches over 30 minutes. Top graph: In growing branches, Ppk1::sfGFP
1140 signal was quantified as a percentage of the branch length marked by CD4::tdTomato (de novo:
1141 11 branches, 4 neurons; existing: 18 branches, 5 neurons). Ppk1::sfGFP was present along the
1142 entire length of the branch. Bottom graph: In 30 minutes, both newly formed and existing
1143 branches grew equivalent lengths (de novo: 11 branches, 4 neurons; existing: 19 branches, 5
1144 neurons). (C) Still images (top) and kymographs (bottom) from a 3-minute movie of GFP
1145 fluorescence from Ppk1::GFP(11x3)^{EC} in a growing dendrite tip marked by CD4::tdTomato.
1146 Arrowheads point to initial and final locations of dendrite growth. Genotype:
1147 *Ppk1::GFP(11x3)^{EC}/DcG-Gal4; UAS-secGFP(1-10)/ppk-CD4::tdTomato*. Scale bars, 3 μm. (D)
1148 Representative images and quantification of FRAP of GFP in neurons expressing
1149 Ppk1::GFP(11x3)^{EC}::mCherry$^{C\text{-term}}$ and GFP(11)^{EC}::CD4::tdTomato (both genotypes: 8 neurons,
1150 8 larvae). Quantification, percent recovery: Student's unpaired t-test, 1 min (p=0.5417), 3 min
1151 (p=0.0108), 5 min (p=0.0064); 10 min (p<0.0001); 20 min (p=0.0021). In the image montage,
1152 dashed lines represent the bleached region, which was within 50-150 μm of the cell body. The
1153 GFP signal in a 10 μm section centered in the bleached region was quantified at each of the
1154 indicated time points. Scale bar, 10 μm. (E) Representative images and quantification of control
1155 neurons (*w^{1118}*; 12 neurons, 5 larvae) and neurons lacking both Ppk1 and Ppk26 (Δppk1
1156 [*ppk1$^{attP\text{-}KO/attP\text{-}KO}$*]; Δppk26 [*ppk26$^{\Delta 11/\Delta 11}$*]; 8 neurons, 4 larvae). Quantification, dendrite length:
1157 Student's unpaired t-test (p=0.9783). Quantification, dendrite tip number: Student's unpaired t-
1158 test (p=0.2592). The neuronal membrane is marked by CD4::GFP (*ppk-CD4::GFP*). Scale bar,

1159 100 μm. In the graphs, each data point represents either a dendrite branch (B) or a neuron (E),

1160 and data are plotted as mean ± SEM. n.s.=not significant ($p>0.05$), *$p<0.05$, **$p=0.01$-0.001,

1161 and ****$p<0.0001$.

1162 **Fig 4. Ppk1 levels are not affected by decreasing dendrite arbor size but are reduced**
1163 **when dendrite length increases.**
1164 Images of ddaC neuron morphology in live 2nd instar larvae (72 h AEL). The dendritic membrane
1165 is marked by CD4::tdTomato, unless otherwise noted. Zoomed inset images show Ppk1::sfGFP
1166 in segments of dendrite in live 3rd instar larvae (120 h AEL). (A) Representative images and
1167 quantification of control and *Rpl22-RNAi*-expressing neurons. Quantification, dendrite length:
1168 Student's unpaired t-test (p<0.0001); control (13 neurons, 6 larvae) v. *Rpl22-RNAi* (13 neurons,
1169 5 larvae). Dendrite length of *Rpl22-RNAi*-expressing neurons was quantified using Ppk1::sfGFP
1170 because the CD4::tdTomato signal was too dim to analyze in these mutants. Quantification,
1171 dendrite tip number: Mann-Whitney test (p<0.0001); control (13 neurons, 6 larvae) v. *Rpl22-*
1172 *RNAi* (13 neurons, 5 larvae). Quantification, Ppk1::sfGFP, dendrites: Student's unpaired t-test
1173 (p=0.8602); control (20 neurons, 9 larvae) v. *Rpl22-RNAi* (27 neurons, 14 larvae). (B)
1174 Representative images and quantification of control and *EcR-DN*-expressing neurons.
1175 Quantification, dendrite length: Student's unpaired t-test (p<0.0001); control (15 neurons, 9
1176 larvae) v. *EcR-DN* (15 neurons, 7 larvae). Quantification, dendrite tip number: Student's
1177 unpaired t-test (p<0.0001); control (15 neurons, 9 larvae) v. *EcR-DN* (15 neurons, 7 larvae).
1178 Quantification, Ppk1::sfGFP, dendrites: Student's unpaired t-test (p=0.2318); control (24
1179 neurons, 10 larvae) v. *EcR-DN* (23 neurons, 10 larvae). (C) Representative images and
1180 quantification of control neurons and neurons over-expressing *Rac1* (*Rac1* O/E). Quantification,
1181 dendrite length: Student's unpaired t-test (p=0.7618); control (15 neurons, 10 larvae) v. *Rac1*
1182 O/E (14 neurons, 5 larvae). Quantification, dendrite tip number: Student's unpaired t-test
1183 (p<0.0001); control (15 neurons, 10 larvae) v. *Rac1* O/E (14 neurons, 5 larvae). Quantification,
1184 Ppk1::sfGFP, dendrites: Student's unpaired t-test (p=0.0791); control (20 neurons, 9 larvae) v.
1185 *Rac1* O/E (20 neurons, 9 larvae). (D) Representative images and quantification of control
1186 neurons and neurons over-expressing *PI3K* (*PI3K* O/E). Quantification, dendrite length:
1187 Student's unpaired t-test (p=0.0001); control (12 neurons, 5 larvae) v. *PI3K* O/E (12 neurons, 6

1188 larvae). Quantification, dendrite tip number: Student's unpaired t-test (p=0.0002); control (12
1189 neurons, 5 larvae) v. *PI3K* O/E (12 neurons, 6 larvae). Quantification, Ppk1::sfGFP, dendrites:
1190 Student's unpaired t-test (p<0.0001); control (26 neurons, 14 larvae) v. *PI3K* O/E (22 neurons,
1191 13 larvae). Control genotype: w^{1118}; *ppk-Gal4*. Experimental genotypes: *ppk-Gal4* was used to
1192 express the indicated construct. *CD4::tdTomato* and *Ppk1::sfGFP* included as indicated.
1193 Experiments to analyze the effects of *Rpl22-RNAi* and *Rac1 over-expression* were run together;
1194 the controls for these experiments are the same. In the graphs, each data point represents a
1195 neuron, and data are plotted as mean ± SEM. n.s.=not significant (p>0.05), ***p=0.001-0.0001,
1196 and ****p<0.0001. AU: arbitrary units. Scale bars, 50 μm.
1197
1198

1199 **Fig 5. Ppk1 persists in dendrites when dynein-mediated transport is disrupted, and**
1200 **dynein plays a role transporting Ppk1 away from Golgi.**
1201 Images of ddaC neurons in live 3rd instar larvae. Dashed-outline boxes: zoomed-in views of
1202 dendrite branches, cell bodies, and axons. (A) Representative images and quantification of
1203 Ppk1::sfGFP in control (21 neurons, 11 larvae) and *Dlic-RNAi*-expressing neurons (21 neurons,
1204 11 larvae). Quantification, dendrites: Student's unpaired t-test (p=0.7756). Quantification, axons:
1205 Mann-Whitney test (p<0.0001). Scale bars, 50 μm and 5 μm (dashed-outline boxes). (B)
1206 Representative images and quantification of Ppk1::sfGFP in control neurons and neurons over-
1207 expressing *dmn* (O/E *dmn*). Quantification, dendrites, 72 h AEL: Mann Whitney (p=0.1417);
1208 control (16 neurons, 6 larvae) v. O/E *dmn* (14 neurons, 6 larvae). Quantification, dendrites, 120
1209 h AEL: Student's unpaired t-test (p<0.0001); control (20 neurons, 12 larvae) v. O/E *dmn* (24
1210 neurons, 14 larvae). Quantification, axons, 120 h AEL: Mann-Whitney test (p<0.0001); control
1211 (20 neurons, 12 larvae) v. O/E *dmn* (23 neurons, 14 larvae). Scale bars, 50 μm and 5 μm
1212 (dashed-outline boxes). (C) Representative images of Ppk1::sfGFP and GALNT2::TagRFP in
1213 control and *Dlic-RNAi*-expressing neurons. In *Dlic-RNAi*-expressing neurons, Ppk1::sfGFP
1214 (green arrowheads) accumulates in Golgi in the cell body and Golgi outposts, marked by
1215 GALNT2::TagRFP (magenta arrowheads). Scale bars, 10 μm (solid-outline boxes; dashed-
1216 outline boxes, cell body) and 5 μm (dashed-outline boxes, dendrites). (D) Representative
1217 images of Ppk1::sfGFP and GALNT2::TagRFP in the axons of control and *Dlic-RNAi*-expressing
1218 neurons. Zoomed-in images of an axon of a *Dlic-RNAi*-expressing neuron shows that the
1219 Ppk1::sfGFP puncta (green arrowheads) do not colocalize with ectopic Golgi marked by
1220 GALNT2::TagRFP (magenta arrowheads). Scale bars, 10 μm and 5 μm (dashed-outline boxes).
1221 (E) Representative images of GALNT2::TagRFP and Ppk1::sfGFP in the axons of control and
1222 Lva-DN-expressing neurons. In Lva-DN, GALNT2::TagRFP mislocalizes to axons (blue
1223 arrowheads) and axonal Ppk1::sfGFP levels increase. Quantification, Ppk1::sfGFP, axons:
1224 Student's unpaired t-test (p<0.0001); control (17 neurons, 6 larvae) v. Lva-DN (16 neurons, 7

1225 larvae). Scale bar, 10 μm. Control genotypes: *w*^{1118}; *ppk-Gal4*. Experimental genotypes: *w*^{1118};

1226 *ppk-Gal4 UAS-Dlic-RNAi UAS-Dicer* (A, C, D), *w*^{1118}; *ppk-Gal4 UAS-dmn* (B), *w*^{1118}; *ppk-Gal4*

1227 *UAS-Lva-DN* (E). *UAS-GALNT2::TagRFP* and *Ppk1::sfGFP* included as indicated (A-E). In the

1228 graphs, each data point represents a neuron and data are plotted as mean ± SEM. n.s.=not

1229 significant ($p>0.05$) and ****$p<0.0001$. AU: arbitrary units.

1230 **Fig 6. Disrupting secretory pathway function reduces both dendrite growth and**
1231 **membrane-expressed Ppk1.**
1232 Images of ddaC neurons in live 3rd instar larvae. Dashed-outline boxes: zoomed-in views of
1233 dendrite branches. (A) Representative images and quantification of neuron morphology in
1234 control (12 neurons, 6 larvae) and *Sec23-gRNA*-expressing (12 neurons, 5 larvae) neurons. The
1235 neuronal membrane is marked by CD4::tdTomato. Quantification, dendrite length: Mann-
1236 Whitney test ($p<0.0001$). Quantification, dendrite tip number: Student's unpaired t-test
1237 ($p<0.0001$). Scale bar, 100 μm. (B) Representative images and quantification of
1238 Ppk1::GFP(11x3)^{EC}::mCherry$^{C\text{-}term}$ in control and *Sec23-gRNA*-expressing neurons.
1239 Quantification, reconstituted GFP, dendrites: Student's unpaired t-test ($p<0.0001$); control (18
1240 neurons, 8 larvae) v. *Sec23-gRNA* (12 neurons, 8 larvae). Quantification, mCherry, dendrites:
1241 Student's unpaired t-test ($p=0.0039$); control (18 neurons, 8 larvae) v. *Sec23-gRNA* (14
1242 neurons, 8 larvae). Quantification, mCherry, axons: Student's unpaired t-test ($p=0.0002$); control
1243 (17 neurons, 8 larvae) v. *Sec23-gRNA* (13 neurons, 8 larvae). Scale bars, 50 μm and 10 μm
1244 (dashed-outline boxes). (C) Representative images and quantification of Ppk1::sfGFP in control
1245 and *Sec23-gRNA*-expressing neurons. Quantification, dendrites: Student's unpaired t-test
1246 ($p=0.1414$); control (26 neurons, 15 larvae) v. *Sec23-gRNA* (20 neurons, 11 larvae).
1247 Quantification, axons: Student's unpaired t-test ($p<0.0001$); control (26 neurons, 15 larvae) v.
1248 *Sec23-gRNA* (16 neurons, 10 larvae). Scale bars, 50 μm and 10 μm (dashed-outline boxes).
1249 Control genotypes: *w^{1118}*; *ppk-Cas9*. Experimental genotype: *w^{1118}*; *ppk-Cas9 U6-Sec23-gRNA*.
1250 *ppk-CD4::tdTomato*, *Ppk1::GFP(11x3)^{EC}::mCherry$^{C\text{-}term}$*, and *Ppk1::sfGFP* included as indicated
1251 (A-C). In the graphs, each data point represents a neuron, and data are plotted as mean ± SEM.
1252 n.s.=not significant ($p>0.05$), **$p=0.01$-0.001, ***$p=0.001$-0.0001, and ****$p<0.0001$. AU:
1253 arbitrary units.

1254 **Fig 7. Normal dendritic levels of Ppk1 rely on Rab11.**

1255 Images of ddaC neurons in 3rd instar larvae, fixed (A, D) or live (B, C, E). Dashed-outline boxes:
1256 zoomed-in images of cell bodies. (A) Representative images and quantification of membrane-
1257 expressed Ppk1, recognized by anti-Ppk1 antibodies, in control (18 neurons, 6 larvae) and
1258 *Rab11-RNAi*^{108382}-expressing neurons (18 neurons, 6 larvae). (B) Representative images and
1259 quantification of Ppk1::sfGFP in the dendrites and cell bodies of control (23 neurons, 18 larvae)
1260 and *Rab11-RNAi*^{108382}-expressing neurons (24 neurons, 12 larvae). (C) Representative images
1261 and quantification of Ppk1::mCherry in the dendrites of control (20 neurons, 10 larvae) and
1262 *Rab11-RNAi*^{108382}-expressing neurons (23 neurons, 11 larvae). (D) Representative image and
1263 quantification of membrane-expressed Ppk1, recognized by anti-Ppk1 antibodies, in control (19
1264 neurons, 6 larvae) and *Rab11-DN*-expressing neurons (18 neurons, 6 larvae). In ddaC neurons
1265 expressing Rab11-DN, Ppk1 immunostaining in the cell body was frequently observed (blue
1266 arrowhead). (E) Representative images and quantification of Ppk1::mCherry in control (28
1267 neurons, 12 larvae) and *Rab11-DN*-expressing neurons (28 neurons, 14 larvae). Control
1268 genotype: *w*^{1118}; *ppk-Gal4*. Experimental genotypes: *w*^{1118}; *ppk-Gal4 UAS-Rab11-RNAi*^{108382} (A-
1269 C) and *w*^{1118}; *ppk-Gal4 UAS-Rab11-DN::GFP* (D, E). *Ppk1::sfGFP* or *Ppk1::mCherry* included
1270 as indicated (A-E). -Tx: no Triton X-100 (non-permeabilizing conditions). In the graphs, each
1271 data point represents a neuron, and data are plotted as mean ± SEM. Quantification: Student's
1272 unpaired t-test. ****$p<0.0001$. AU: arbitrary units. Scale bars, 50 μm and 10 μm (dashed-outline
1273 boxes).

1274 **Fig 8. Ppk1::mCherry puncta colocalize with Rab5::GFP, but dendritic levels of Ppk1 do**
1275 **not depend on Rab5 function.**
1276 Images of ddaC neurons in 3rd instar larvae, live (A, C) or fixed (B). Dashed-outline boxes:
1277 zoomed-in views of dendrite branch and cell bodies. (A) Representative images of
1278 Ppk1::mCherry with Rab5::GFP. Arrowheads: Colocalized signal. Zoomed-in view of
1279 Ppk1::mCherry and Rab5::GFP in a dendrite branch. Line trace is through the punctum
1280 highlighted by the arrowhead. Zoomed-in view of Ppk1::mCherry and Rab5::GFP in the cell
1281 body and proximal dendrites. (B) Representative images and quantification of membrane-
1282 expressed Ppk1, recognized by anti-Ppk1 antibodies, in control neurons (14 neurons, 6 larvae)
1283 and neurons over-expressing wild-type *Rab5* (Rab5-WT; 19 neurons, 6 larvae) or *Rab5-DN* (16
1284 neurons, 6 larvae). Quantification: one-way ANOVA with post-hoc Tukey; control v. *Rab5-WT*
1285 (p=0.1323), control v. *Rab5-DN* (p=0.1562), and *Rab5-WT* v. *Rab5-DN* (p=0.9999). (C)
1286 Representative images and quantification of Ppk1::mCherry in control (20 neurons, 10 larvae)
1287 and *Rab5-DN*-expressing neurons (20 neurons, 10 larvae). Quantification, Ppk1::mCherry
1288 levels, dendrite: Student's t-test (p=0.1782). Quantification, Ppk1::mCherry puncta number:
1289 Mann-Whitney test (p<0.0001). Ppk1::mCherry puncta were quantified in dendrites within 70 μm
1290 of the cell body. Control genotype: w^{1118}; *ppk-Gal4*. Experimental genotype: w^{1118}; *ppk-Gal4*
1291 *UAS-Rab5-DN::YFP* (B, C). *UAS-Rab5::GFP*, *UAS-Rab5::YFP* (Rab5-WT OE), and
1292 *Ppk1::mCherry* included as indicated (A-C). -Tx: no Triton X-100 (non-permeabilizing
1293 conditions). In the graphs, each data point represents a neuron, and data are plotted as mean ±
1294 SEM. n.s.=not significant (p<0.05) and ****p<0.0001. AU: arbitrary units. Scale bars, 50 μm and
1295 10 μm (dashed-outline boxes).

1296 **Supporting information**

1297

1298 **S1 Fig. Effects of tagging endogenous Ppk1 on Ppk1 levels.**

1299

1300 **S2 Fig. Endogenous Ppk1 tagged with sfGFP at two different sites in an extracellular loop**

1301 **and Ppk1 tagged extracellularly with pHluorin.**

1302

1303 **S3 Fig. Characterization of a split-GFP approach to label membrane-expressed Ppk1.**

1304

1305 **S4 Fig. Characterization of GFP(11)^{EC}::CD4::tdTomato.**

1306

1307 **S5 Fig. Aberrant Pickpocket channel activity disrupts dendrite morphogenesis.**

1308

1309 **S6 Fig. Disrupting Rab11 levels or activity causes a reduction in dendrite arbor growth.**

1310

1311 **S7 Fig. Wild-type Rab5 and Rab5-DN show a different pattern of distribution, and Rab5-**

1312 **DN reduces dendritic arbor morphogenesis.**

Figure 1

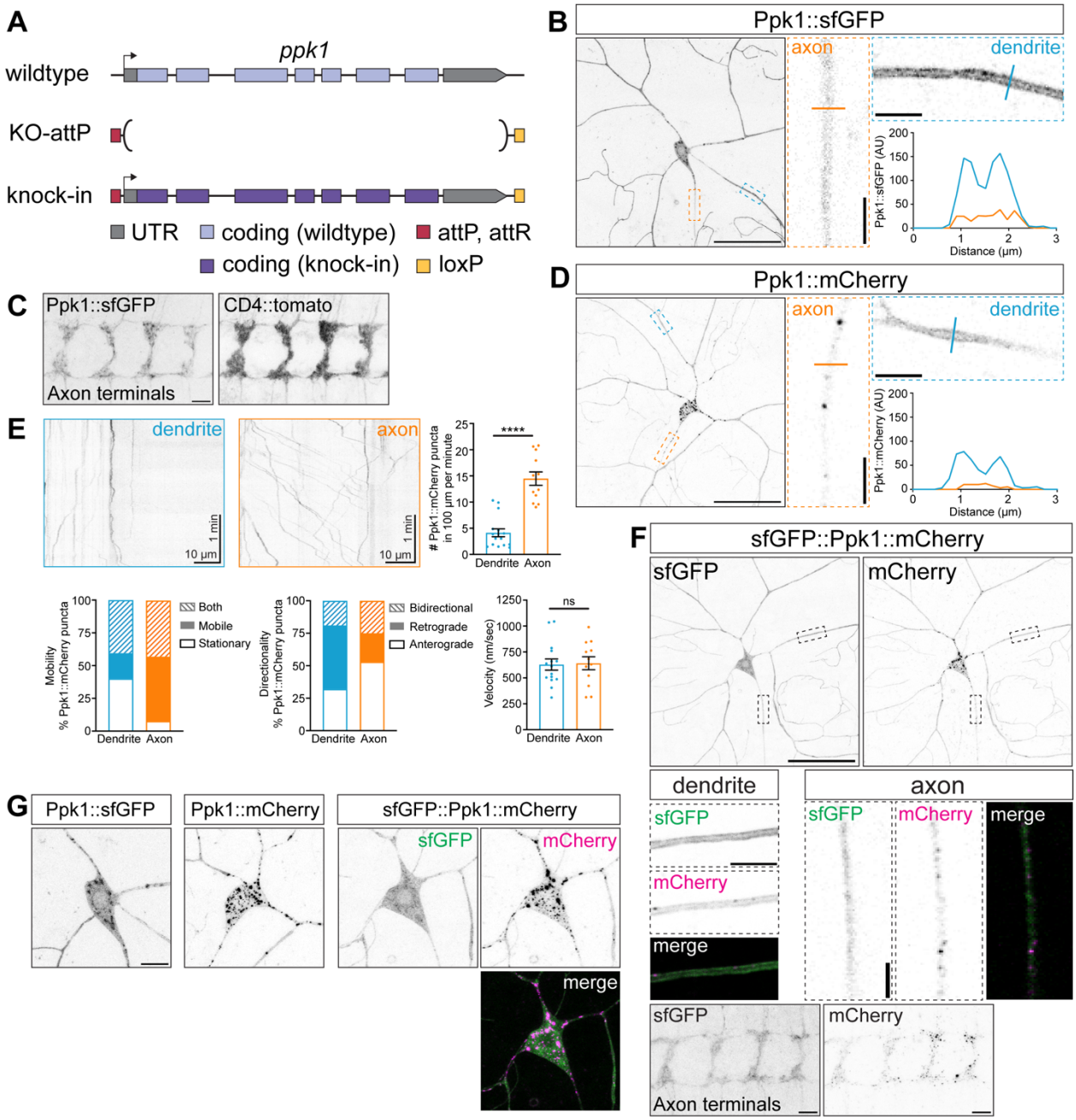
A
ppk1
wildtype
KO-attP
knock-in
UTR
coding (wildtype)
attP, attR
coding (knock-in)
loxP
B
Ppk1::sfGFP
axon
dendrite
Ppk1::sfGFP (AU)
Distance (µm)
C
Ppk1::sfGFP
CD4::tomato
Axon terminals
D
Ppk1::mCherry
axon
dendrite
Ppk1::mCherry (AU)
Distance (µm)
E
dendrite
axon
1 min
10 µm
Ppk1::mCherry puncta in 100 µm per minute
****
Dendrite
Axon
Mobility
% Ppk1::mCherry puncta
Both
Mobile
Stationary
Directionality
Bidirectional
Retrograde
Anterograde
Velocity (nm/sec)
ns
F
sfGFP::Ppk1::mCherry
sfGFP
mCherry
dendrite
axon
merge
Axon terminals
G
Ppk1::sfGFP
Ppk1::mCherry
sfGFP::Ppk1::mCherry
sfGFP
mCherry
merge

Figure 2

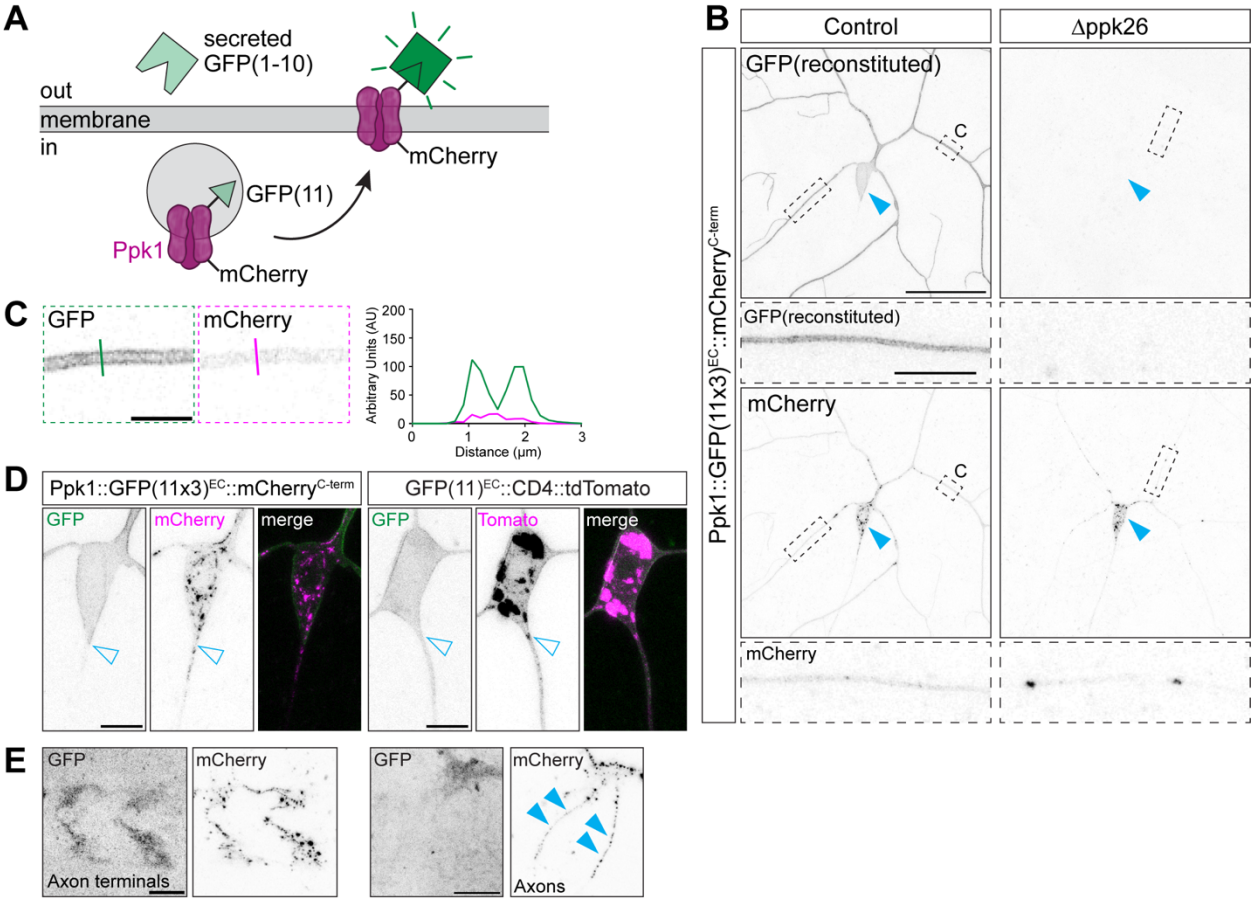
A
secreted
GFP(1-10)
out
membrane
in
mCherry
GFP(11)
Ppk1
mCherry
B
Control
Δppk26
Ppk1::GFP(11x3)EC::mCherryC-term
GFP(reconstituted)
C
GFP(reconstituted)
mCherry
C
mCherry
C
GFP
mCherry
Arbitrary Units (AU)
200
150
100
50
0
0
1
2
3
Distance (μm)
D
Ppk1::GFP(11x3)EC::mCherryC-term
GFP(11)EC::CD4::tdTomato
GFP
mCherry
merge
GFP
Tomato
merge
E
GFP
mCherry
Axon terminals
GFP
mCherry
Axons

Figure 3

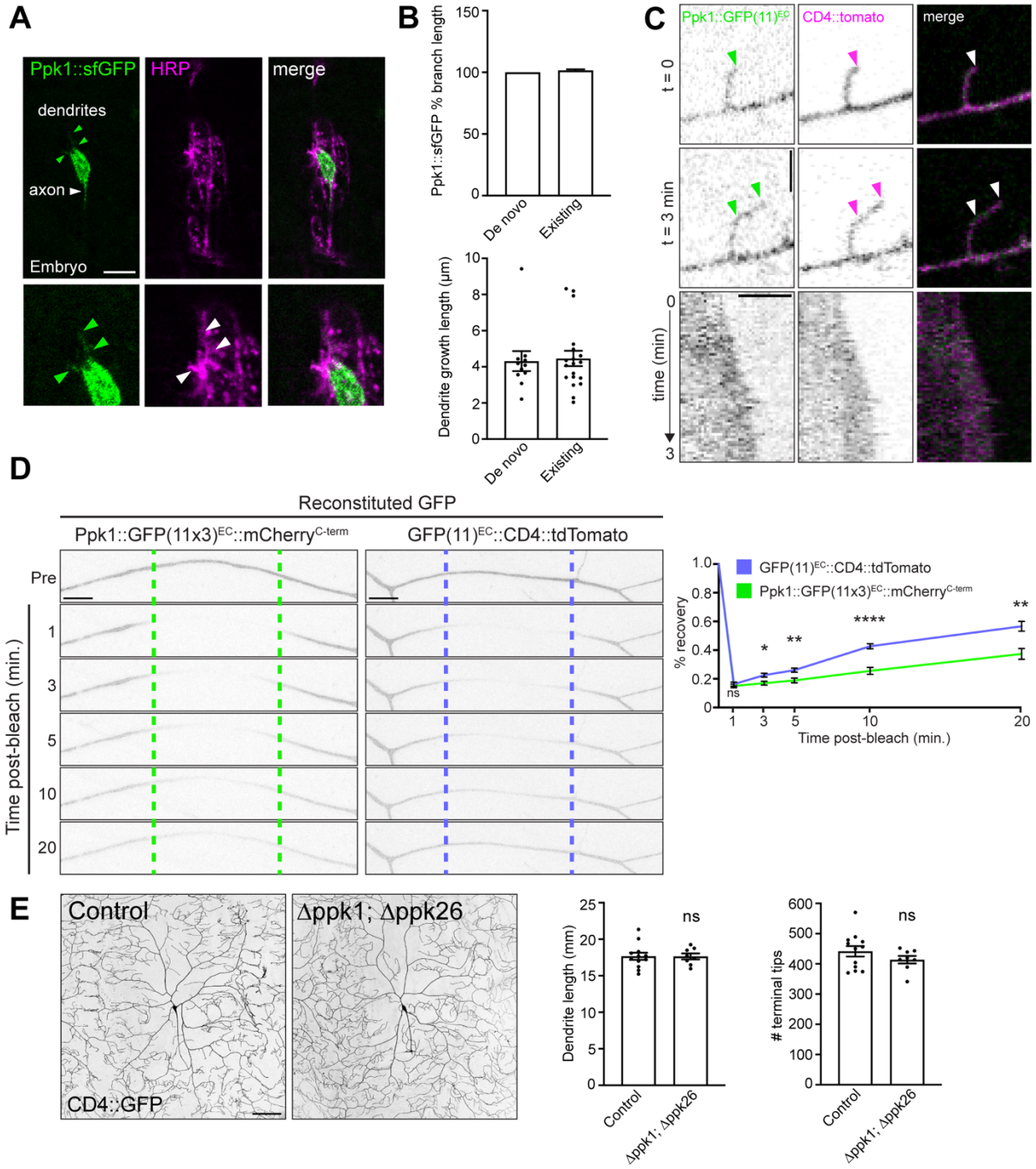
A
Ppk1::sfGFP
HRP
merge
dendrites
axon
Embryo
B
Ppk1::sfGFP % branch length
150
100
50
0
De novo
Existing
Dendrite growth length (µm)
10
8
6
4
2
0
De novo
Existing
C
Ppk1::GFP(11)EC
CD4::tomato
merge
t = 0
t = 3 min
time (min)
0
3
D
Reconstituted GFP
Ppk1::GFP(11x3)EC::mCherryC-term
GFP(11)EC::CD4::tdTomato
Pre
Time post-bleach (min.)
1
3
5
10
20
GFP(11)EC::CD4::tdTomato
Ppk1::GFP(11x3)EC::mCherryC-term
% recovery
1.0
0.8
0.6
0.4
0.2
0
ns
*
**
****
**
1
3
5
10
20
Time post-bleach (min.)
E
Control
Δppk1; Δppk26
CD4::GFP
Dendrite length (mm)
25
20
15
10
5
0
ns
Control
Δppk1; Δppk26
terminal tips
600
500
400
300
200
100
0
ns
Control
Δppk1; Δppk26

Figure 4

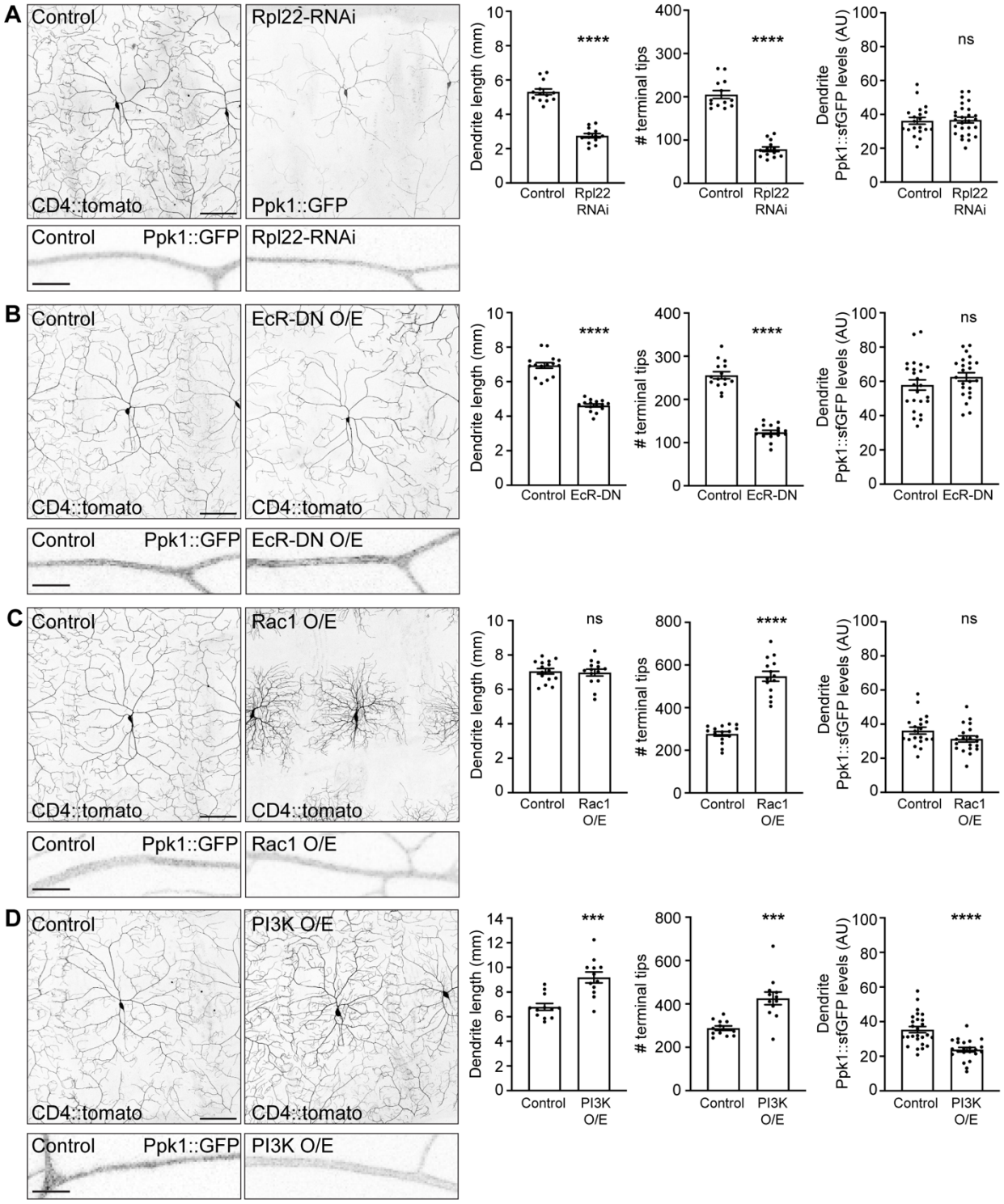
A
Control
Rpl22-RNAi
CD4::tomato
Ppk1::GFP
Control
Ppk1::GFP
Rpl22-RNAi
Dendrite length (mm)
****
Control
Rpl22 RNAi
terminal tips
****
Control
Rpl22 RNAi
Dendrite Ppk1::sfGFP levels (AU)
ns
Control
Rpl22 RNAi
B
Control
EcR-DN O/E
CD4::tomato
CD4::tomato
Control
Ppk1::GFP
EcR-DN O/E
Dendrite length (mm)
****
Control
EcR-DN
terminal tips
****
Control
EcR-DN
Dendrite Ppk1::sfGFP levels (AU)
ns
Control
EcR-DN
C
Control
Rac1 O/E
CD4::tomato
CD4::tomato
Control
Ppk1::GFP
Rac1 O/E
Dendrite length (mm)
ns
Control
Rac1 O/E
terminal tips
****
Control
Rac1 O/E
Dendrite Ppk1::sfGFP levels (AU)
ns
Control
Rac1 O/E
D
Control
PI3K O/E
CD4::tomato
CD4::tomato
Control
Ppk1::GFP
PI3K O/E
Dendrite length (mm)
***
Control
PI3K O/E
terminal tips
***
Control
PI3K O/E
Dendrite Ppk1::sfGFP levels (AU)
****
Control
PI3K O/E

Figure 5

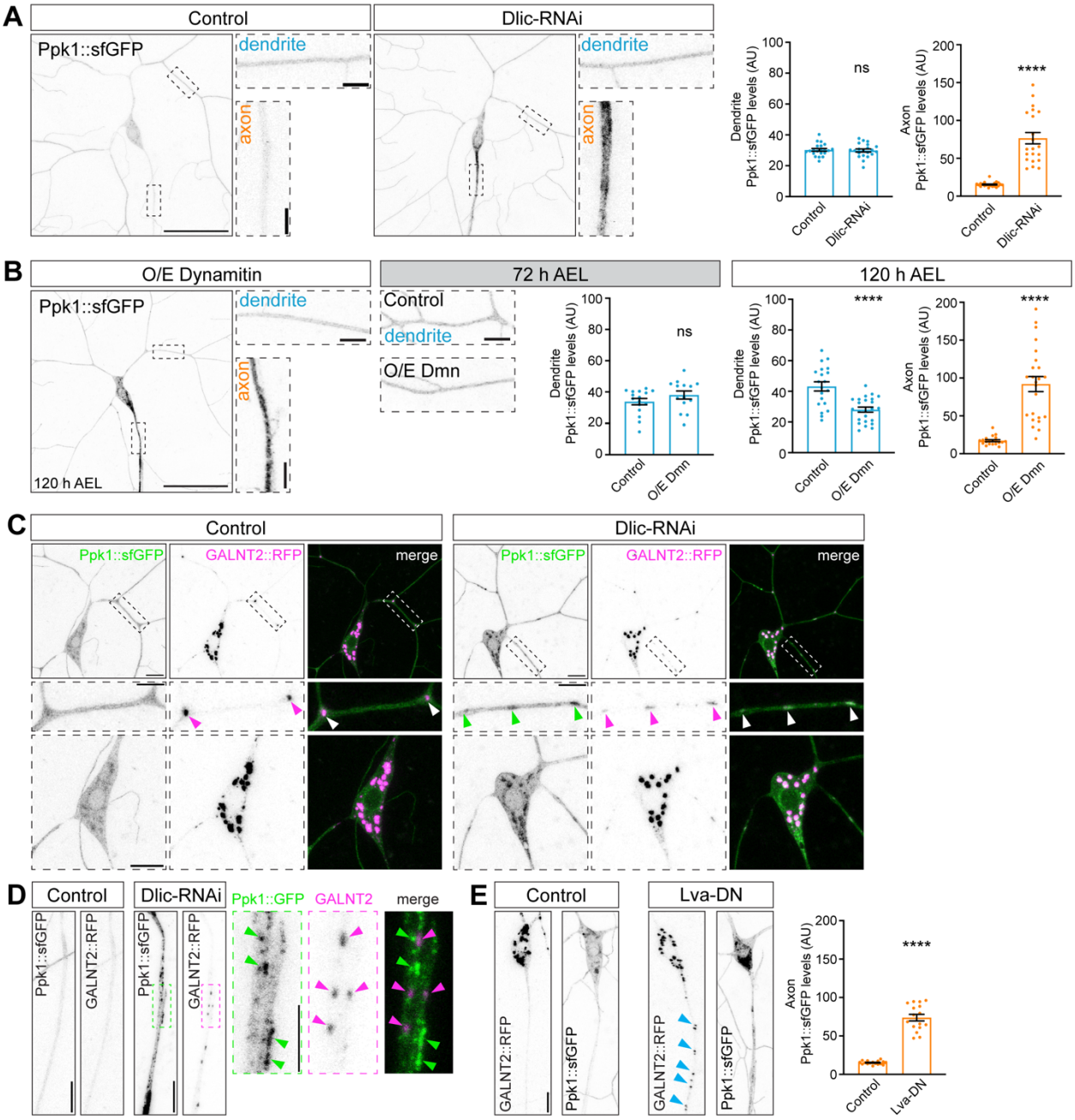
A
Control
Dlic-RNAi
Ppk1::sfGFP
dendrite
axon
Dendrite Ppk1::sfGFP levels (AU)
Axon Ppk1::sfGFP levels (AU)
ns
****
Control
Dlic-RNAi
B
O/E Dynamitin
72 h AEL
120 h AEL
O/E Dmn
120 h AEL
C
GALNT2::RFP
merge
D
Ppk1::GFP
GALNT2
E
Lva-DN

Figure 6

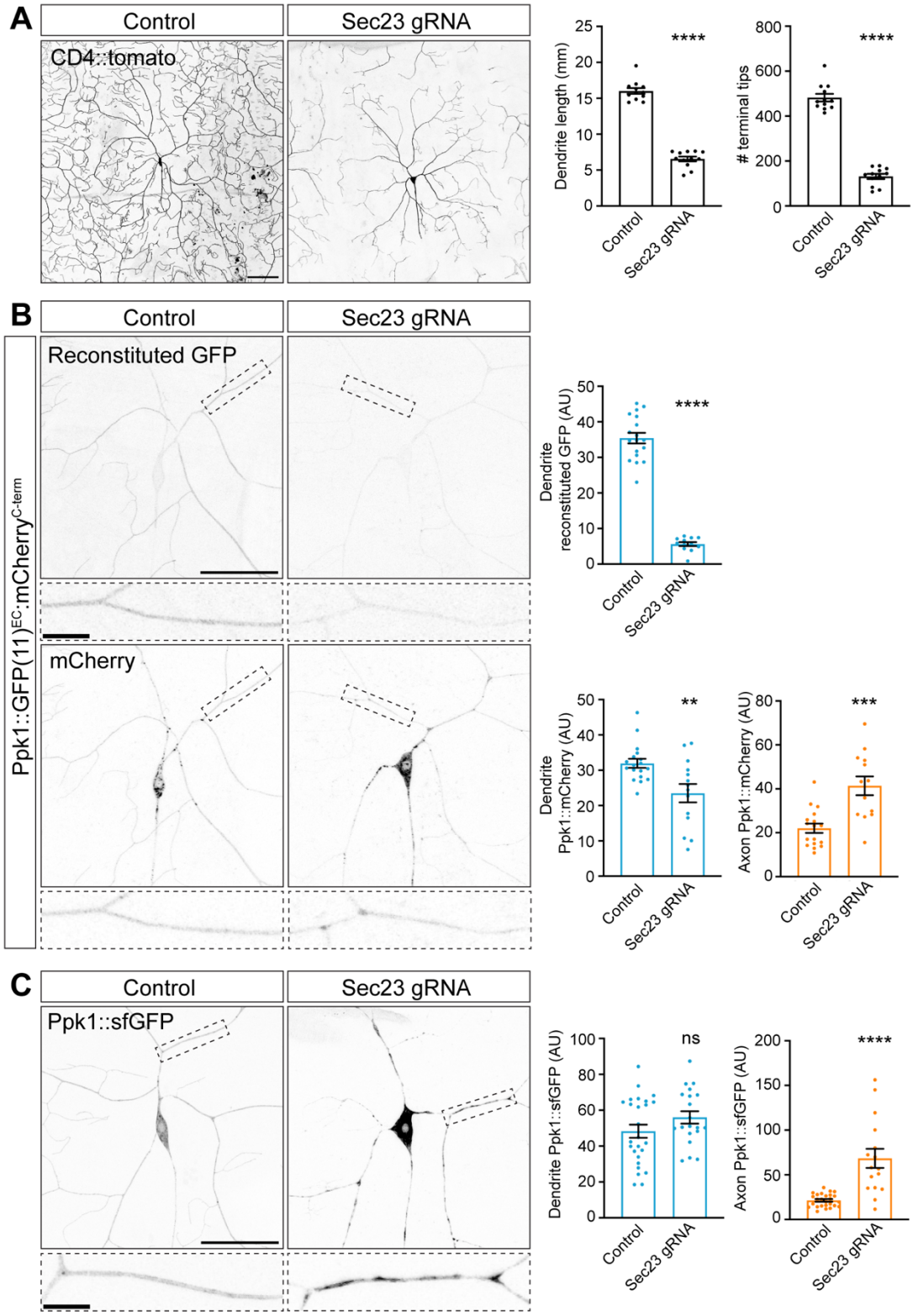
A
Control
Sec23 gRNA
CD4::tomato
Dendrite length (mm)
****
terminal tips
****
Control
Sec23 gRNA
B
Control
Sec23 gRNA
Ppk1::GFP(11)EC:mCherryC-term
Reconstituted GFP
Dendrite reconstituted GFP (AU)
****
mCherry
Dendrite Ppk1::mCherry (AU)
**
Axon Ppk1::mCherry (AU)
***
C
Control
Sec23 gRNA
Ppk1::sfGFP
Dendrite Ppk1::sfGFP (AU)
ns
Axon Ppk1::sfGFP (AU)
****

Figure 7

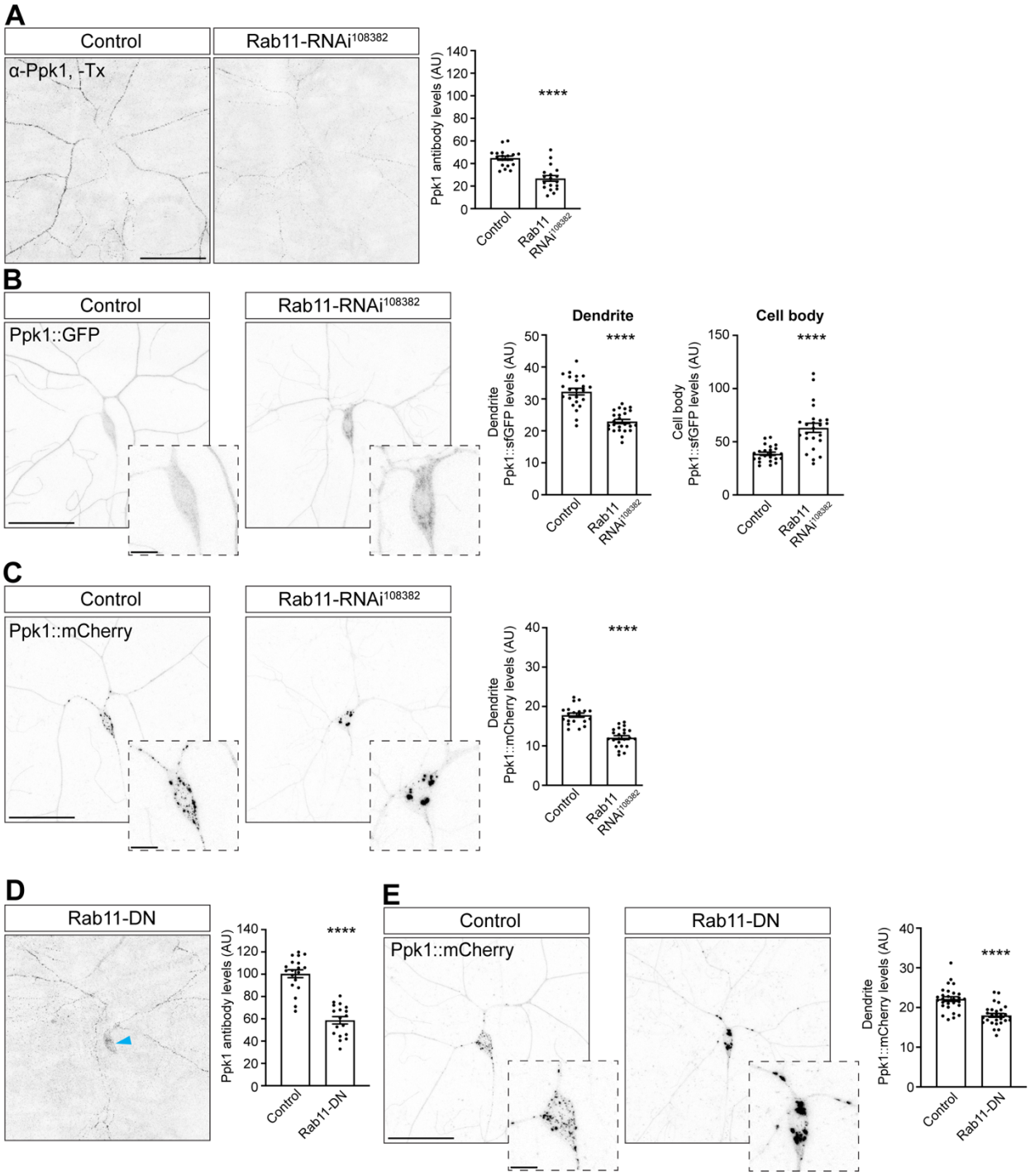
A
Control
Rab11-RNAi108382
α-Ppk1, -Tx
Ppk1 antibody levels (AU)
****
Control
Rab11 RNAi108382
B
Control
Rab11-RNAi108382
Ppk1::GFP
Dendrite
Dendrite Ppk1::sfGFP levels (AU)
Cell body
Cell body Ppk1::sfGFP levels (AU)
C
Control
Rab11-RNAi108382
Ppk1::mCherry
Dendrite Ppk1::mCherry levels (AU)
D
Rab11-DN
Ppk1 antibody levels (AU)
Control
Rab11-DN
E
Control
Rab11-DN
Ppk1::mCherry
Dendrite Ppk1::mCherry levels (AU)

Figure 8

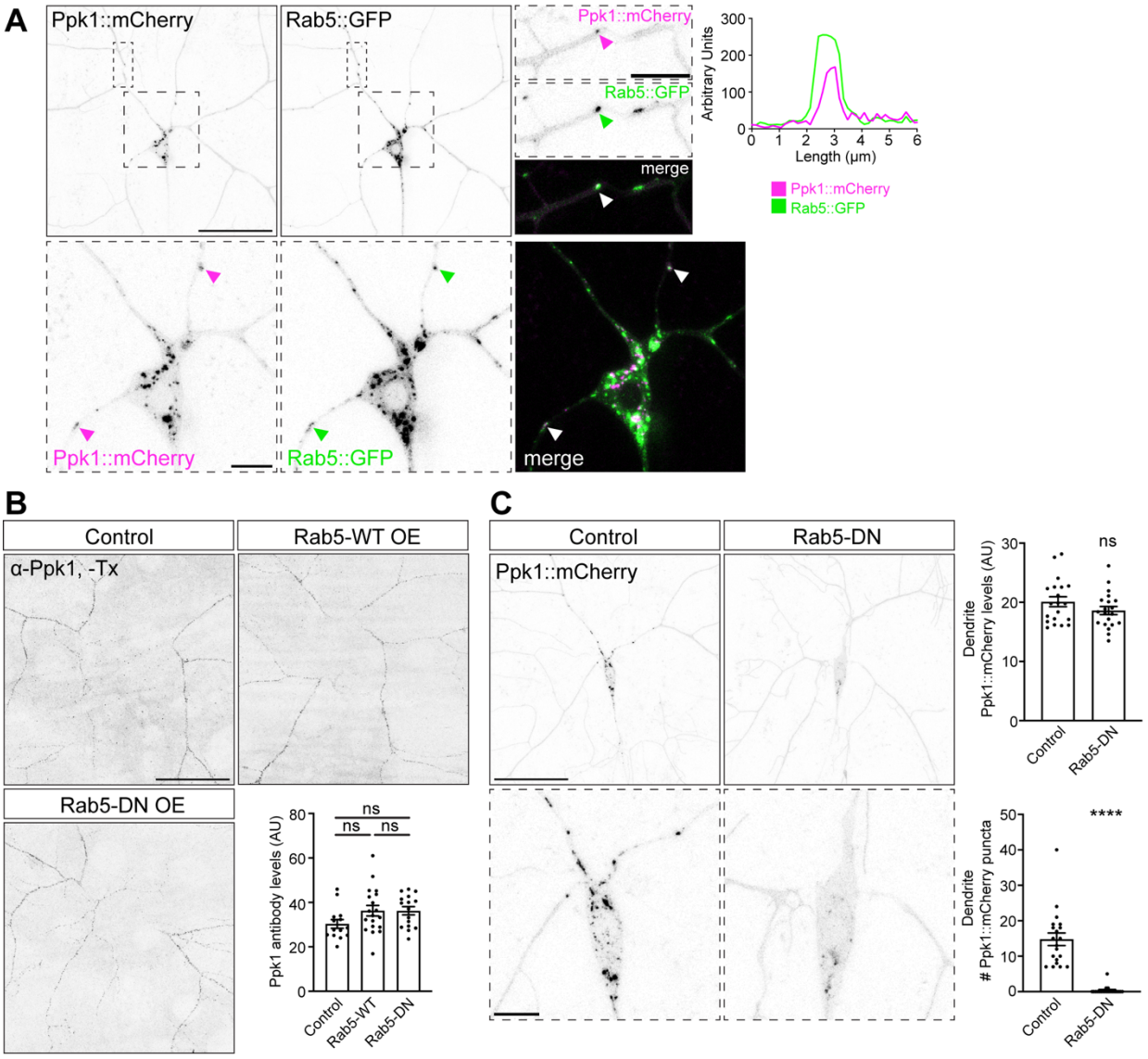
A
Ppk1::mCherry
Rab5::GFP
merge
Arbitrary Units
Length (μm)
B
Control
Rab5-WT OE
α-Ppk1, -Tx
Rab5-DN OE
Ppk1 antibody levels (AU)
ns
Control
Rab5-WT
Rab5-DN
C
Rab5-DN
Dendrite Ppk1::mCherry levels (AU)
Ppk1::mCherry puncta
****